Tribological Behaviors of Vacuum Hot-Pressed Ceramic Composites with Enhanced Cyclic Oxidation and Corrosion Resistance

Xuewu Li [a,b,c], Jingsong Liang [a], Tian Shi [a,*], Danni Yang [a], Xinchun Chen [b,*], Chuanwei Zhang [a], Zhaohui Liu [d], Dianzi Liu [e], Qiaoxin Zhang [d,*]

[a] School of Mechanical Engineering, Xi'an University of Science and Technology, Xi'an 710054, China

[b] State Key Laboratory of Tribology, Tsinghua University, Beijing 100084, China

[c] Shandong Key Laboratory of Corrosion Science, Institute of Oceanology, Chinese Academy of Sciences, Qingdao 266071, China

[d] School of Mechanical and Electronic Engineering, Wuhan University of Technology, 122 Luoshi Road, Wuhan 430070, China

[e] Engineering Division, Faculty of Science, University of East Anglia, Norwich NR4 7TJ, England

*Corresponding authors.

E-mail addresses: tianshi@xust.edu.cn (T. Shi), chenxc1213@mail.tsinghua.edu.cn (X.C. Chen), zhangqx@whut.edu.cn (Q.X. Zhang)

ABSTRACT

Wear failure is a bottleneck restricting applications and developments of Ti_3SiC_2 ceramic. Particles reinforced composites provide an effective strategy to resist wear. In this work, $Ti(C,N)$ particles are used as reinforcements, and $Ti_3SiC_2/Ti(C,N)$ composite is fabricated by vacuum hot-pressing. Scanning electron microscopy (SEM), energy dispersive spectrometer (EDS) and X-ray diffract meter (XRD) are used to investigate composite morphologies, compositions and phases before and after hot-pressing. Meanwhile, high-temperature cyclic oxidations and tribological behaviors of composites under various loads, speeds and $Ti(C,N)$ contents are characterized. Results show that as-prepared composite is relatively dense, and $Ti(C,N)$ addition plays an important role in particle reinforcement of Ti_3SiC_2. Meanwhile, its hardness, wear resistance, cyclic oxidation resistance and corrosion resistance are significantly improved. In addition, wear characteristics and mechanisms of composites under different loads and speeds are analyzed in details. This work shows great potentials in developing engineering applications of ceramics, especially in high-temperature, oxidizing, frictional and corrosive environments.

Keywords: Ceramic material; Wear resistance; Cyclic oxidation; Particle reinforcement; Corrosion resistance

1. Introduction

Ti$_3$SiC$_2$ ceramic is widely used in high-temperature structural components [1,2], electrical contact parts [3-5], welding parts [6], nuclear components [7,8], rotating equipments [9,10] and anti-corrosion layers [11,12] due to excellent physical, chemical and mechanical behaviors [13,14]. Ti$_3$SiC$_2$ has prominent metallic properties [15], such as good thermal conductivity, electrical conductivity and ductility at room temperature [16]. It also possesses excellent ceramic behaviors, such as high yield strength, high melt point, high thermal stability, thermal-shock resistance and high strength [17]. More important, it can be processed by traditional machining, which is different from carbide ceramic [18]. Meanwhile, it has lower friction coefficient and superior self lubrication than molybdenum disulfide and graphite [19,20]. Such special behaviors make Ti$_3$SiC$_2$ widely used in electromechanical, instrumental, metallurgical, chemical, automotive, marine, national-defense and aerospace fields.

Ti$_3$SiC$_2$ also shows good high-temperature oxidation resistance and cyclic oxidation resistance. Li et al. [21] have investigated oxidability of Ti$_3$SiC$_2$ after oxidizing at 1000-1500 °C for 20 h. Results show double-layer films with various compositions form on surface. The outer layer composes of TiO$_2$, and the inner composes of SiO$_2$ and TiO$_2$. Both dense films are difficult to fall off at high temperature, and also display excellent oxidation resistance. Liu et al. [22] have discussed cyclic oxidation resistance of Ti$_3$SiC$_2$. It is found that obvious oxide layer composing of titanium dioxides form on surface after cyclic oxidation at 1100 °C. Furthermore, few cracks develop on oxide layer suggesting that Ti$_3$SiC$_2$ acts out excellent resistance to

3

high-temperature cyclic oxidation.

Under dry friction condition, contact regions of Ti_3SiC_2 ceramic only occur on its protrusions [23-25]. Elastic deformation of contact regions gradually turns into plastic deformation, resulting in continuously increased contact areas. Such ceramic suffers severe adhesive wear and aggravated abrasion due to its poor plastic deformation with growth of friction speed and load [26-28]. Generally, friction coefficient of Ti_3SiC_2 is larger than 0.5 in case of dry friction [29,30]. Friction heat gradually accumulates on ceramic, causing a continuous temperature rise on grinding surface [31,32]. As a result, cracks and grain fractures develop on ceramic under such heat effect. In addition, micro pores inevitably occur on Ti_3SiC_2, which brings about stress concentration, reduced ceramic strength and hardness [33]. Hence, wear resistance of Ti_3SiC_2 ceramic at high temperature is seriously threatened, which limits its applications in engineering fields.

Ti(C,N) is a promising ceramic with prominent physical, chemical and mechanical properties, such as acid-alkali resistance, high melting point, high strength, high hardness, good chemical stability, corrosion resistance and wear resistance [34,35], which exactly compensates for shortcomings of Ti_3SiC_2. Herein, Ti_3SiC_2 powders are prepared by pressureless sintering at 1400 °C. Then with the aid of vacuum hot-pressing, Ti_3SiC_2/Ti(C,N) material is achieved. Results show that as-prepared composite exhibits superior resistances to wear, oxidation and corrosion. This work sheds positive insights in fabricating multifunctional ceramic composites for fulfilling engineering needs that traditional materials cannot meet under high-temperature,

oxidizing, frictional and corrosive environments.

2. Materials and methods

2.1 Materials

Table 1 shows average granularities and purities of raw materials used in this work. Ti, SiC, TiC, Al and Ti(C,N) powders were purchased from Haocheng Metal Co., Ltd., Shanghai, China. Other reagents used with analytical grades were provided by Shaanxi Chemical Industry Co., Ltd., Xi'an, China.

2.2 Procedures

Powders were mixed according to a stoichiometric ratio of $n(Ti):n(SiC):n(TiC):n(Al)=4:2:1:0.2$. Ball milling was processed by placing mixed powders and absolute ethanol in a vacuum stainless steel tank installed on planetary ball mill. In milling process, grinding ball was made of stainless steel, ball to powder weight ratio was 4:1, grinding time was 24 h and rotating speed was 200 r/min. After milling and drying, homogeneously mixed reactants were obtained. Then reactants were put in an alumina crucible and sintered in a vacuum furnace (ZT-15-20, Chenhua Electric Furnace Co., Ltd., Shanghai, China) at 1280 °C. After grinding sintered products with agate bowl, Ti_3SiC_2 powders were achieved.

Ti(C,N) powders with various mass fractions (5, 10, 15, 20 wt%) were mixed with the resultant Ti_3SiC_2. The maximum Ti(C,N) mass fraction of 20 wt% was achieved by optimizing composite hardness. After adding absolute ethanol and milling for 24 h, uniformly mixed slurry was achieved, and homogeneously reactants were obtained with further drying and passing through a 120 mesh sieve. Then compaction treatment

5

was conducted by adding reactants in a circular stainless steel mold on a tablet machine (FYD, Sitron Precision Technology Development Co., Ltd., Tianjin, China) with 30 MPa molding pressure and 4% paraffin molding agent. After drying in air, dewaxing was proceeded in an argon atmosphere furnace at 400 °C for 1 h with a temperature rise rate of 5 °C/min. Then dewaxed mixture was placed in a vacuum carbon tube furnace and sintered with a temperature rise rate of 10 °C/min at 1250, 1300, 1350 and 1400 °C. The maximum sintering temperature of 1400 °C was determined by optimizing composite hardness. Heat preservation was kept for 1 h after sintering. Finally, Ti_3SiC_2/Ti(C,N) composite was achieved after cooling in vacuum condition.

2.3 Characterization

X-ray diffract meter (XRD, D/MAX-RB, Japan), scanning electron microscopy (SEM, JSM-5610LV, Japan) and energy dispersive spectrometer (EDS, Phoenix, USA) were used to analyze chemical phases, micro morphologies and surface compositions, respectively. Polarization curve and electrochemical impedance spectroscopy were obtained by electrochemical workstation (CHI660E, China) for characterizing corrosion resistances of Ti_3SiC_2/Ti(C,N) composites. Polarization curve was recorded from -0.5 to 2.5 V with 1 mV/s scan rate. Impedance spectrum was recorded with 10 mV amplitude from 10^{-2} to 10^5 Hz. Vickers hardness tester (HVS-1000, China) was used to measure sample hardness with an applied pressure of 10 N for 10 s. The final hardness was achieved by averaging three measurements. Measured density (ρ_m) of sample was determined using Archimedes principle [36]:

$$\rho_{\mathrm{m}} = \frac{A}{A-B}\left(\rho_1 - \rho_2\right) + \rho_2 \tag{1}$$

where ρ_1 and ρ_2 respectively referred to auxiliary liquid density and air density (0.0012 g/cm^3), A and B denoted to sample masses in air and auxiliary liquid, respectively. Theoretical density (ρ_{t}) was calculated according to the composite rule [37]:

$$\rho_{\mathrm{t}} = \frac{\rho_{\mathrm{a}}\rho_{\mathrm{b}}}{n_{\mathrm{a}}\rho_{\mathrm{b}} + n_{\mathrm{b}}\rho_{\mathrm{a}}} \tag{2}$$

where ρ_{a} and ρ_{b} respectively represented theoretical densities of Ti$_3$SiC$_2$ and Ti(C,N), n_a and n_{b} respectively indicated mass percentages of Ti$_3$SiC$_2$ and Ti(C,N). Relative density (ρ_{r}) of composite was expressed as:

$$\rho_{\mathrm{r}} = \frac{\rho_{\mathrm{m}}}{\rho_{\mathrm{t}}} \times 100\% \tag{3}$$

High-temperature ball-disk friction and wear tester (HT-1000, Zhongke Kaihua Technology Development Co., Ltd., Lanzhou, China) was used for tribological test. GCr15 steel ball with 5 mm diameter was used. Before test, as-prepared composite was polished by buffing machine, and then ultrasonically cleaned with absolute ethanol. The test was processed under room-temperature and dry-friction conditions for 20 min with 3 mm rotation radius. Comparative experiments were also conducted under various loads and rotation speeds. Instantaneous friction coefficient was measured and averaged as the final friction coefficient. Wear rate (W) was determined by weighing mass changes before and after friction test, which was related to mass loss (ΔM), test load (N) and sliding distance (S):

$$W = \frac{\Delta M}{NS} \tag{4}$$

Ti$_3$SiC$_2$/Ti(C,N) composite obtained from vacuum hot-pressing was cut into strips by wire electrical-discharge machining, then polished, ultrasonically cleaned and dried. Al$_2$O$_3$ crucible was also ultrasonically cleaned with absolute ethanol to remove impurities and oil stains. Ti$_3$SiC$_2$/Ti(C,N) composite was put in Al$_2$O$_3$ crucible for incubating at 800, 1000 and 1200 °C for 50 min in box furnace. Afterwards, it was cooled in drying oven for 10 min. The above process represented an oxidation cycle. Finally, mass changes before and after oxidation were calculated for determining relationships with cycle numbers and analyzing composite oxidation kinetics.

3. Results and discussion

3.1 Composition, structure and property of Ti$_3$SiC$_2$/Ti(C,N) composite

Fig. 1 shows SEM image and XRD pattern of Ti$_3$SiC$_2$ powders. As seen, as-prepared powders display plate-like hexagonal-crystal structures, and they are uniformly distributed with sizes of about 5-10 μm. The main diffraction peaks in XRD results are corresponding to Ti$_3$SiC$_2$ materials. Meanwhile, a small amount of TiC peaks are observed, suggesting that as-prepared powders mainly compose of Ti$_3$SiC$_2$ besides slight TiC materials.

Fig. 2a shows XRD patterns of Ti$_3$SiC$_2$/Ti(C,N) composites sintered at 1400 °C with different Ti(C,N) mass fractions. XRD patterns of Ti$_3$SiC$_2$/Ti(C,N) materials sintered with 20 wt% Ti(C,N) at various temperatures are illustrated in Fig. 2b. It is seen that the main components of as-prepared composites are Ti$_3$SiC$_2$ and Ti(C,N) accompanied by small amounts of SiC and TiC. Meanwhile, a relatively dense composite surface is achieved after sintering at 1400 °C with 20 wt% Ti(C,N), as seen

in **Fig. 2c**. **Fig. 2d** and **e** are corresponding to cross-section SEM images of the sample in **Fig. 2c**. As seen, typical plate-like structures fracturing along cleavage planes are Ti_3SiC_2 phases. It is also found that fine Ti(C,N) particles distribute in Ti_3SiC_2 matrix.

Fig. 3a depicts measured densities and relative densities of composites sintered with 20 wt% Ti(C,N) at different temperatures. Clearly, relative density increases with sintering temperature. As temperature rises, shrinkage force generated from sintered body is enhanced leading to an increased material density [38]. Measured densities and relative densities of composites sintered at 1400 °C with various Ti(C,N) mass fractions are displayed in **Fig. 3b**. As seen, both densities increase with Ti(C,N) content. Since Ti(C,N) density is higher than that of Ti_3SiC_2, composite density increases as Ti(C,N) content rises.

Fig. 4a displays the relationship between sintering temperature and micro hardness of Ti_3SiC_2/Ti(C,N) composites with 20 wt% Ti(C,N). It is seen that composite hardness increases with sintering temperature. As mentioned above, sample density showing positive correlation with hardness enhances with sintering temperature, so composite hardness also increases with temperature. However, composite hardness decreases when sintering temperature achieves 1450 °C. Such an exorbitant temperature makes Ti(C,N) particles gather in molten body, resulting in uneven heating of ceramic composite. Then composite hardness decreases under actions of reinforcement aggregation and thermal runaway. Therefore, the maximum sintering temperature of 1400 °C can be finally determined by optimizing composite hardness.

Fig. 4b exhibits composite hardness sintered at 1400 °C with different Ti(C,N) mass fractions. As seen, micro hardness increases with Ti(C,N) mass fraction. When Ti(C,N) mass fraction increases to 20 wt%, a greatly enhanced hardness of 6.81 GPa is achieved. As typical hard phases [39], the addition of Ti(C,N) ceramics acting as particles for reinforcing Ti_3SiC_2 matrix significantly increases composite hardness. However, composite hardness decreases when Ti(C,N) mass fraction exceeds 20 wt%. Exorbitant Ti(C,N) content makes melt viscosity rise and fluidity decline. As a result, composite porosity and impurity increase, directly leading to the decrease of composite density and hardness. Hence, the maximum Ti(C,N) mass fraction of 20 wt% is achieved by optimizing composite hardness.

3.2 Effect of Ti(C,N) content on tribological property

Instantaneous friction coefficients versus time for composites with different Ti(C,N) contents at low speed (0.1 m/s) and light load (5 N) are achieved in **Fig. 5a**. **Fig. 5b** shows instantaneous friction coefficients versus time for composites with different Ti(C,N) contents at high speed (0.4 m/s) and heavy load (20 N). Comparatively, larger fluctuations of friction coefficients are found for high speeds and heavy loads. Furthermore, both fluctuation ranges of composites with high Ti(C,N) contents are larger than the low ones, and the same is true for friction coefficients.

Fig. 6a and **b** respectively exhibit average friction coefficients and wear rates versus Ti(C,N) contents for composites at various speeds and loads. Under a low speed and light load condition, friction coefficient increases first and then decreases, but the corresponding wear rate decreases as Ti(C,N) content increases. Under a high

speed and heavy load condition, both friction coefficient and wear rate increase with

Ti(C,N) contents.

Under a low speed (0.1 m/s) and light load (5 N) condition, **Fig. 7a** and **b** show

surface morphologies of frictional composites with Ti(C,N) contents of 5 and 20 wt%,

respectively. More and deeper furrows are found in **Fig. 7a**, suggesting that low

Ti(C,N) content is easy to develop plastic deformation on composite for its inadequate

material hardness thereby making a poor resistance to furrows in the case of low

speed and light load [40]. Hence, friction coefficient of composite increases and wear

rate is large at this stage. For a high Ti(C,N) content in **Fig. 7b**, however, relatively

shallow furrows are observed. When Ti(C,N) content is high, it is hard to produce

plastic deformation on composite for its enhanced hardness thereby making a strong

resistance to furrows. So the corresponding friction coefficient gradually decreases,

and wear rate is small, which is consistent with the data trends in **Fig. 5** and **6**.

Under a high speed (0.4 m/s) and heavy load (20 N) condition, **Fig. 8a** and **b**

display surface morphologies of frictional composites with Ti(C,N) contents of 5 and

20 wt%, respectively. **Fig. 8c** and **d** correspond to EDS spectra of composites in **Fig.**

8a and **b**, respectively. Rough transfer fragments with numerous Fe elements are

found in **Fig. 8a** and **c**. It shows that Fe elements in steel ball transfer and adhere to

composite surface during frictional process thereby resulting in severe adhesive wear.

When Ti(C,N) content reaches 20 wt% (**Fig. 8b**), composite surface is relatively

smooth accompanied by some groove marks, transfer fragments and pits induced by

particle detachment. Meanwhile, Fe and O elements develop on surface (**Fig. 8d**)

indicating that both adhesive wear and oxidative wear occur in frictional process. The increase of frictional speed will cause a sharp rise of surface temperature [41]. Furthermore, temperature distribution and stress distribution are uneven on such a rough contact surface. Therefore, for a low Ti(C,N) content, load-carrying micro protrusions produce plastic deformation and adhesive wear thereby resulting in low friction coefficient and wear rate. For a high Ti(C,N) content, it will cause adhesive wear and oxidative wear of micro protrusions. Under further action of frictional shear force, hard phases in composite are peeled off as abrasive particles, eventually leading to furrow formation, increased friction coefficient and wear rate, as exhibited in **Fig. 5** and **6**.

3.3 Effect of load and speed on tribological property

Friction coefficients and wear rates versus applied loads for composites with 20 wt% Ti(C,N) at different speeds are achieved in **Fig. 9a** and **b**, respectively. As seen, friction coefficients decrease with the increase of loads, but wear rates increase with loads at 0.1 m/s. Both friction coefficients and wear rates decrease as loads increase at 0.2 m/s. At speeds of 0.3 and 0.4 m/s, friction coefficients and wear rates decrease first and then increase with loads.

Under a heavy load condition (20 N), **Fig. 10a** and **b** display surface morphologies of frictional composites with 20 wt% Ti(C,N) at 0.1 and 0.2 m/s, respectively. **Fig. 10c** and **d** respectively refer to EDS spectra of composites in **Fig. 10a** and **b**. Few furrows are found on composite for its high Ti(C,N) content and micro hardness, as shown in **Fig. 10a**. But transfer fragments and a small amount of film products are

12

observed on surface. More film products are also seen in **Fig. 10b**. The corresponding

EDS spectrum shows that the main elements of films are Ti, Si, Al and O indicating

mixtures of Ti, Si and Al oxides. There is also slight Fe element suggesting mild

adhesive wear on composite surface. At 0.1 m/s, plastic deformation occurs on

composite surface so that its friction coefficient decreases with the increase of load,

while wear rate increases with load. Meanwhile, abrasive wear mainly occurs at this

stage. At 0.2 m/s, more oxide films form on composite making friction coefficient and

wear rate decrease with the increase of load. Therefore oxide film wear mainly occurs

at this stage [42].

Under a rotation speed of 0.3 m/s, **Fig. 11a** and **b** show surface morphologies of

frictional composites with 20 wt% Ti(C,N) at 5 and 15 N, respectively. **Fig. 11c** and **d**

respectively display enlarged SEM images of **Fig. 11a** and **b**. **Fig. 11e** and **f** exhibit

EDS spectra of composites in **Fig. 11a** and **b**, respectively. As seen, oxide films also

form on composites. Compared with low speeds (**Fig. 10**), such films are more

uniform, continuous and dense, suggesting that frictional surfaces are easier to oxidize

as speeds increase. By observing enlarged image in **Fig. 11c**, oxide film covered with

a small amount of particles is uniform and continuous at 5 N. These particles act as

abrasive grains for forming micro grooves on film. At 15 N, cracks develop on oxide

film (**Fig. 11d**), which may be fatigue cracks under cyclic stress [43]. The increase of

load tends to destroy oxide film at 0.3 m/s. As seen in EDS spectra (**Fig. 11e-f**), the

main components of oxide films on frictional surfaces are Ti, Si, O and Fe. With

increases in speed and load, O and Fe contents raise indicating aggravated oxidation

on composite and intensified element transfer between friction pairs. Under low load conditions, friction coefficients and wear rates decrease as loads increase because of oxide films, which play key roles in lubricating interfaces. Meanwhile, oxide film wear occurs on composite. When applied load reaches 15 N, cracks develop on composite. As load continues to increase, composite surface is subject to severe adhesive wear, and oxide film is damaged. Combining with shearing action, hard phases in composites are peeled off to form micro pits. Hard phases also act as abrasive particles in friction process, and abrasive wear occurs [44,45]. As a result, both friction coefficient and wear rate of composites increase with loads. The above tribological behaviors versus applied loads at 0.3 m/s are in accordance with the rotation speed of 0.4 m/s.

3.4 Oxidation resistance of Ti$_3$SiC$_2$/Ti(C,N) composite

Fig. 12 shows the relationship between mass increments and oxidation cycle times of Ti$_3$SiC$_2$/Ti(C,N) composites with 20 wt% Ti(C,N) at different oxidation temperatures. As seen, mass increments increase with cycle times. Cyclic oxidation process includes three stages. The first stage corresponds to the first 5 cycles. Oxide film forms quickly at this stage, exhibiting a sharp oxidation process. The second stage is from 5 to 35 cycles, in which oxidation mass increment rate is on the decline. At this stage, a dense oxide film forms on composite thereby slowing down its oxidation rate. The third stage indicates the cycle more than 35 times. At this stage, mass increment tends to be stable, because oxide film on surface is too dense to carry out oxidation reaction [46].

Fig. 13a displays XRD patterns of oxide layers on composites after 40 oxidation cycles at various temperatures. At 800 °C, oxide layer composes of TiO_2, SiO_2 and slight Ti_3SiC_2, indicating that composite has been oxidized. At 1000 °C, intensified TiO_2 diffraction peak and weakened Ti_3SiC_2 peak suggest aggravated oxidation extent on surface. At 1200 °C, TiO_2 diffraction peak is significantly enhanced, but Ti_3SiC_2 peak almost disappear, demonstrating that Ti_3SiC_2 phase has been oxidized to form a thick oxide film. **Fig. 13b** shows XRD patterns of oxide layers on composites after different oxidation cycles at 1000 °C. As shown, after 5 cycles, the main phase is Ti_3SiC_2, but TiO_2 peak is also observed, indicating that composite surface has been oxidized. After 20 cycles, the main diffraction peak is TiO_2 accompanied by slight SiO_2 and almost vanished Ti_3SiC_2 peak, suggesting relatively sufficient oxidation on composite. After 40 cycles, the distribution of diffraction peaks on surface is basically the same as that of 20 cycles, indicating that oxide film composition has not changed [47]. The above analyses are consistent with previous experimental results in **Fig. 12**.

Fig. 14a-c show SEM images of oxide layers on composites after 40 oxidation cycles at 800, 1000 and 1200 °C, respectively. **Fig. 14d** and **e** refer to EDS spectra of composites in **Fig. 14a** and **c**, respectively. As seen, oxide layer thicknesses at 800, 1000 and 1200 °C are respectively about 20-30, 70-80 and 120-130 μm, which increase with temperatures. It is also observed that Si element disappears and Ti element increases, indicating that Ti_3SiC_2 is continuously oxidized to form TiO_2 when temperature rises from 800 to 1200 °C [48]. As a result, oxide layer thickens gradually, which is consistent with the above experimental results and analysis.

15

Fig. 15a-c exhibit cross-section SEM images of oxide layers on composites after 40 oxidation cycles at 800, 1000 and 1200 °C, respectively. At 800 °C, Ti_3SiC_2 is oxidized to form a thin oxide film, and also its oxide grains are about 0.5 μm wide and 3 μm long. At 1000 °C, oxide grains display clear outlines and sharp edges, which is due to freely grown grains without applied pressures during sintering. Meanwhile, owing to different growth environments and growth rates of grains, gaps form between grains leading to a loose oxide film [49]. Gaps also act as diffusion channels of oxygen atoms thereby causing rapidly oxidized composite surface, and the corresponding grain size is larger than that at 800 °C. At 1200 °C, TiO_2 growth presents a lamellar epitaxy trend, and preferred orientation is obvious suggesting that TiO_2 crystal grows outwards. Similarly, gaps also form between grains leading to oxygen atom diffusions for developing oxidation reaction. Finally, a gradually thickened oxide film comes into being.

3.5 Corrosion resistance of Ti_3SiC_2/Ti(C,N) composite

Polarization curves recorded from -0.5 to 2.5 V with 1 mV/s scan rate for Ti_3SiC_2/Ti(C,N) composites sintered at 1400 °C with various Ti(C,N) mass fractions are achieved by electrochemical workstation in **Fig. 16a**. As seen, anode curves display obvious inflection points at about 0.50 V, and then go through downward trends. All samples also exhibit passivating characterizations. After being fitted with Tafel extrapolation method [50], electrochemical parameters including corrosion potentials and current densities are achieved in **Fig. 16a**. Samples with high corrosion potentials and low current densities generally possess weak electron transfers thereby

leading to superior corrosion resistances [51]. Corrosion inhibition rate (η) is also

used to evaluate corrosion resistances of composites:

$$\eta = \frac{I_a - I_b}{I_a} \times 100\% \tag{5}$$

where I_a and I_b stand for corrosion current densities of samples. The equation

indicates that when Ti(C,N) content increases to 20 wt%, a greatly enhanced

corrosion resistance ($\eta = 86.51\%$) is achieved over Ti_3SiC_2 ceramic, and also

corrosion resistances of composites increase with Ti(C,N) contents.

To further characterize corrosion resistances of composites, electrochemical

impedance spectra are recorded with 10 mV amplitude from 10^{-2} to 10^5 Hz in **Fig.**

16b. As seen, the largest capacitive arc for 20 wt% Ti(C,N) indicates the weakest

charge transfer as well as greatly enhanced corrosion resistance, which is consistent

with polarization result. On the one hand, composite density increases with Ti(C,N)

content, and its addition acts as particles for reinforcing Ti_3SiC_2 matrix. On the other

hand, as a typical hard phase, Ti(C,N) significantly improves composite hardness and

corrosion resistance. In general, Ti(C,N) reinforcements have effectively enhanced

wear resistance, high-temperature cyclic oxidation resistance and corrosion resistance

of Ti_3SiC_2 ceramics.

4. Conclusions

Ti_3SiC_2/Ti(C,N) composites have been prepared in this work. The corresponding

mechanical properties, tribological behaviors, high-temperature oxidation resistances

and corrosion resistances have been investigated. The conclusions are as follows:

(1) The main phases in vacuum hot-pressed composites are Ti_3SiC_2 and Ti(C,N).

17

Ti$_3$SiC$_2$ phase shows plate-like hexagonal-crystal structures, and Ti(C,N) phase exhibits granular characteristic thereby playing a role of particle reinforcement. Sintering temperature and Ti(C,N) content have great influences on composite density and hardness. Measured density, relative density and hardness of composites increase with sintering temperatures, and also they increase with Ti(C,N) contents.

(2) Under rotation speeds of 0.1-0.4 m/s and applied loads of 5-20 N, friction coefficients of composites with 20 wt% Ti(C,N) change within a range of 0.33-0.58, while wear rates in a range of 0.50-4.76$\times10^{-6}$ g/Nm. Improved wear resistances of composites are mainly due to the increase of material hardness induced by Ti(C,N) additions and the formation oxide films with good lubricating properties. Surface films mainly compose of mixed oxides of titanium and silicon. At low speed and light load conditions, plastic deformation occurs on composite leading to abrasive wears. As loads and speeds increase, wear mechanisms convert into adhesive wears, and it also shows boundary lubrication friction with oxide films.

(3) Oxidation extent of composite surface increases with temperatures and oxidation cycles. Cyclic oxidation process includes three stages. The first stage corresponds to a sharp oxidation process. At the second stage, a dense oxide film forms on surface thereby slowing down its oxidation rate. At the third stage, oxidation mass increment tends to be stable, because oxide film on surface is too dense to carry out oxidation reaction. Meanwhile, high-temperature grain growth is also along with material oxidation.

(4) Corrosion resistances of composites increase with Ti(C,N) contents. Ti(C,N)

18

additions act as particles for reinforcing Ti_3SiC_2 matrix. Meanwhile, as a typical hard phase, Ti(C,N) reinforcement significantly improves composite hardness and corrosion resistance.

Acknowledgements

References

[1] P. Istomin, E. Istomina, A. Nadutkin, V. Grass, Fabrication of Ti_3SiC_2/SiCp multiport minichannel plates for high-temperature applications, J. Eur. Ceram. Soc. 39 (15) (2019) 4602-4608.

[2] H.H. Shen, X. Xiang, H.B. Zhang, X.S. Zhou, H.X. Deng, X.T. Zu, Effects of helium irradiation dose and temperature on the damage evolution of Ti_3SiC_2 ceramic, Chinese Physics B 28 (7) (2019) 076104.

[3] X.C. Huang, Y. Feng, G. Qian, Z.J. Zhou, Arc ablation properties of Ti_3SiC_2 material, Ceram. Int. 45 (16) (2019) 20297-20306.

[4] L.L. Zheng, X.C. Li, Q.S. Hua, Z.Q. Dai, T.Z. Zhang, Y.H. Qian, J.J. Xu, M.S. Li, Long-term oxidation and electrical behavior of Nb-doped Ti_3SiC_2 as solid oxide

fuel cell interconnects, J. Am. Ceram. Soc. 100 (7) (2017) 3155-3164.

[5] J.L. Lu, N. Abbas, J.N. Tang, R.T. Hu, G.M. Zhu, Characterization of Ti_3SiC_2-coating on stainless steel bipolar plates in simulated proton exchange membrane fuel cell environments, Electrochem. Commun. 105 (2019) 106490.

[6] Y. Wang, Y.H. Xia, Z.W. Yang, D.P. Wang, Interfacial Microstructure and Properties of Brazed Joints of Ti_3SiC_2 Ceramic and TC4 Alloy, Rare Metal Mat. Eng. 48 (9) (2019) 3041-3047.

[7] H.L. Zhang, R.R. Su, L.Q. Shi, D.J. O'Connor, B.V. King, E.H. Kisi, The damage evolution of He irradiation on Ti_3SiC_2 as a function of annealing temperature, J. Eur. Ceram. Soc. 38 (4) (2018) 1253-1264.

[8] W.A. Hanson, M.K. Patel, M.L. Crespillo, Y.W. Zhang, W.J. Weber, Influence of electronic vs nuclear energy loss in radiation damage of Ti_3SiC_2, Acta Mater. 161 (2018) 302-310.

[9] C. Ang, S. Zinkle, C. Shih, C. Silva, N. Cetiner, Y. Katoh, Phase stability, swelling, microstructure and strength of Ti_3SiC_2-TiC ceramics after low dose neutron irradiation, J. Nucl. Mater. 483 (2017) 44-53.

[10] Y. Wang, X.F. Wu, Z.W. Yang, Y.H. Xia, D.P. Wang, Microstructure and mechanical properties of Ti_3SiC_2/Ti_3SiC_2 diffusion bonded joints using Ti foil as an interlayer, Ceram. Int. 45 (16) (2019) 20900-20909.

[11] Y. Jiang, Y.H. He, Electrochemical corrosion behavior of micrometer-sized porous Ti_3SiC_2 compounds in NaCl solution, Mater. Corros. (2019) 1-6.

[12] X.L. Liu, Y. Jiang, H.B. Zhang, Y.H. He, Corrosion behavior of porous Ti_3SiC_2

in nitric acid and aqua regia, T. Nonferr. Metal. Soc. 27 (3) (2017) 584-590.

[13] F. Turki, H. Abderrazak, F. Schoenstein, F. Tetard, M. Abdellaoui, N. Jouini, Physico-chemical and mechanical properties of Ti_3SiC_2-based materials elaborated from SiC/Ti by reactive spark plasma sintering, J. Adv. Ceram. 8 (1) (2019) 47-61.

[14] J.S. Yang, S.M. Dong, C.G. Xu, Mechanical response and microstructure of 2D carbon fiber reinforced ceramic matrix composites with SiC and Ti_3SiC_2 fillers, Ceram. Int. 42 (2) (2016) 3019-3027.

[15] Q.D. Xiao, F. Zhou, S. Wu, Ti_3SiC_2 friction material prepared by novel method of infiltration sintering, Adv. Appl. Ceram. 116 (1) (2017) 2-7.

[16] B.Q. Li, Z.L. Yang, M.F. Chu, Q.Q. Huang, Z.Y. Wang, R. Gao, Y. Zhong, X.X. Liu, L.M. Duan, P.C. Zhang, Ti_3SiC_2/UO_2 composite pellets with superior high-temperature thermal conductivity, Ceram. Int. 44 (16) (2018) 19846-19850.

[17] S. Gupta, M.F. Riyad, Synthesis and tribological behavior of novel UHMWPE-Ti_3SiC_2 composites, Polym. Composite. 39 (1) (2018) 254-262.

[18] M.A. Lagos, C. Pellegrini, I. Agote, N. Azurmendi, J. Barcena, M. Parco, L. Silvestroni, L. Zoli, D. Sciti, Ti_3SiC_2-Cf composites by spark plasma sintering: processing, microstructure and thermo-mechanical properties, J. Eur. Ceram. Soc. 39 (9) (2019) 2824-2830.

[19] X.B. Deng, X.L. Shi, X.Y. Liu, Y.C. Huang, Z. Yan, K. Yang, Y.F. Wang, Effect of Ti_3SiC_2 on tribological properties of M50 matrix self-lubricating composites from 25 to 450 A degrees C, J. Mater. Eng. Perform. 26 (9) (2017) 4595-4604.

[20] C. Magnus, J. Sharp, W.M. Rain forth, The lubricating properties of spark plasma sintered (SPS) Ti_3SiC_2 MAX phase compound and composite, Tribol. T. (2019) 1-13.

[21] S.B. Li, L.F. Cheng, L.T. Zhang, Oxidation behavior of Ti_3SiC_2 at high temperature in air, Mat. Sci. Eng. A-Struct. 341 (1) (2003) 112-120.

[22] G.M. Liu, M.S. Li, Y. Zhang, Y.C. Zhou, Cracking behavior of oxide scale formed on Ti_3SiC_2-based ceramic, Mat. Sci. Eng. A-Struct. 360 (1-2) (2003) 408-414.

[23] S. Mazumder, A. Kumar, B.K. Singh, H. Roy, N. Mandal, Tribological investigation of MgO/Al_2O_3 ceramic composite with the inclusion of nano CuO in dry abrasive wear test, Mater. Res. Express 6 (8) (2019) 085086.

[24] D. Medved, J. Balko, R. Sedlak, A. Kovalcikova, I. Shepa, A. Naughton-Duszova, E. Baczek, M. Podsiadlo, J. Dusza, Wear resistance of ZrB_2 based ceramic composites, Int. J. Refract. Met. H. 81 (2019) 214-224.

[25] W.Z. Zhai, K. Zhou, Nanomaterials in superlubricity, Adv. Funct. Mater. 29 (28) (2019) 1806395.

[26] N.N. Zhao, Y.R. Zhao, Y.Q. Wei, X. Wang, J. Li, Y.H. Xu, F.X. Yan, Z.X. Lu, Friction and wear behavior of TaC ceramic layer formed in-situ on the gray cast iron, Tribol. Int. 135 (2019) 181-188.

[27] S. Sivakumar, B.R. Gollan, K.V. Prajapati, Influence of ZrB_2 hard ceramic reinforcement on mechanical and wear properties of aluminum, Ceram. Int. 45 (6) (2019) 7055-7070.

[28] J.G. Xu, H.B. Yan, D.G. Gu, Friction and wear behavior of polytetrafluoroethylene composites filled with Ti_3SiC_2, Ceram. Int. 61 (2014) 270-274.

[29] Y. Zhao, T.B. Yu, C. Guan, J.Y. Sun, X.F. Tan, Microstructure and friction coefficient of ceramic (TiC, TiN and B_4C) reinforced Ni-based coating by laser cladding, Ceram. Int. 45 (16) (2019) 20824-20836.

[30] W. Chen, K. Wang, X. Liu, N.R. He, H. Xin, W.H. Hao, Investigation of the friction and wear characteristics of Si_3N_4-hBN ceramic composites under marine atmospheric environment, Int. J. Refract. Met. H. 81 (2019) 345-357.

[31] A.G. Steinerian, N.F. Morozov, M.Y. Gutkind, Effect of grain boundary sliding on fracture toughness of ceramic/graphene composites, Mech. Mater. 137 (2019) 103126.

[32] A. Kasyanova, L. Tarutina, J. Lyagaeva, G. Vdovin, D. Medvedev, A. Demin, Thermal and electrical properties of highly dense ceramic materials based on Co-doped $LaYO_3$, JOM-US 71 (11) (2019) 3789-3795.

[33] R. He, Z. Zhou, Z. Qu, X. Cheng, High temperature flexural, tensile strength and oxidation behavior of Ti_3SiC_2 ceramic at 900 degrees C-1300 degrees C in ambient air, J. Test. Eval. 45 (4) (2017) 1150-1158.

[34] A.G. de la Obra, M.J. Sayagues, E. Chicardi, F.J. Gotor, Development of Ti(C,N)-based cermets with (Co,Fe,Ni)-based high entropy alloys as binder phase, J. Alloy. Compd. 814 (2020) 152218.

[35] A.G. de la Obra, F.J. Gotor, E. Chicardi, Effect of the impact energy on the

chemical homogeneity of a (Ti,Ta,Nb)(C,N) solid solution obtained via a mechanically induced self-sustaining reaction, J. Alloy. Compd. 708 (2017) 1008-1017.

[36] S. Hughes, D. Pearce, Investigating sea level rise due to global warming in the teaching laboratory using Archimedes' principle, Eur. J. Phys. 36 (6) (2015) 065033.

[37] S. Madani, N. Charef, A. Hellal, D.L. Garcia, M.F. Garcia, L. Arrar, M.S. Mubarak, Synthesis, density functional theory studies, and sorption properties toward some divalent heavy metal ions of a new polystyrene-supported 4-(5-mercapto-1,3,4-thiadiazol-2-ylimino) pentan-2-one polymer, J. Appl. Polym. Sci. 137 (3) (2020) 48289.

[38] C. Zhang, M.Q. Li, H. Li, The behavior and mechanism of void self-shrinkage in diffusion bonded 1Cr11Ni2W2MoV steel joint: Effect of temperature and void morphology, J. Manuf. Process. 35 (2018) 71-78.

[39] L. von Fieandt, K. Johansson, T. Larsson, M. Boman, E. Lindahl, On the growth, orientation and hardness of chemical vapor deposited Ti(C,N), Thin Solid Films 645 (2018) 19-26.

[40] W.M. Maita, E.T. Akinola, Numerical prediction of tensile yield strength and micro hardness of Ti_6Al_4V alloy processed by constrained bending and straightening severe plastic deformation, Mater. Res. Express 6 (10) (2019) 106560.

[41] S. Venkatachalam, S. Lenfant, M. Depriester, A.H. Sahraoui, D. Hourlier, Heat

treatment of commercial polydimethylsiloxane PDMS precursors: Part II. Thermal properties of carbon-based ceramic nanocomposites, Ceram. Int. 45 (17) (2019) 21505-21511.

[42] J.J. Liu, C.Y. Zhu, G.Q. Li, Effect of graphene/graphene oxide on wear resistance and thermal conductivity of Co-Ni coatings, JOM-US (2019) 10.1007/s11837-019-03865-2.

[43] X.Y. Liu, X.L. Shi, Y.C. Huang, X.B. Deng, G.C. Lu, Z. Yan, B. Xue, Tribological behavior and self-healing functionality of M50 material covered with surface micropores filled with Sn-Ag-Cu, Tribol. Int. 128 (2018) 365-375.

[44] H.Z. Li, W.P. Tong, C. Ma, L.Q. Chen, L. Zuo, Abrasive wear behaviors of high-vanadium alloy steel using the dry sand/rubber wheel apparatus, P. I. Mech. Eng. J-J. Eng. 233 (12) (2019) 1800-1809.

[45] S. Mazumder, B.B. Barad, B.K. Show, N. Mandal, Tribological property enhancement of 3Y-TZP ceramic by the combined effect of CaF_2 and MgO phases, Ceram. Int. 45 (10) (2019) 13447-13455.

[46] A. Radhi, V. Iacobellis, K. Behdinan, A passive oxidation, finite element kinetics model of an ultra-high temperature ceramic composite, Compos. Part B-Eng. 175 (2019) 107129.

[47] L.L. Zheng, Q.S. Hua, X.C Li, M.S. Li, Y.H. Qian, J.J. Xu, J.M. Zhang, Z.M. Zheng, Z.Q. Dai, H.X. Zhang, Investigation on the effect of Nb doping on the oxidation mechanism of Ti_3SiC_2, Corros. Sci. 140 (2018) 374-378.

[48] M. Haftani, M.S. Heydari, H.R. Baharvandi, N. Ehsani, Studying the oxidation

of Ti$_2$AlC MAX phase in atmosphere: A review, Int. J. Refract. Met. H. 61 (2016) 51-60.

[49] N.V. Sevost'yanov, O.V. Basargin, V.G. Maksimov, N.P. Burkovskaya, High-temperature oxidation of Ti$_3$SiC$_2$-based materials prepared by spark plasma sintering, Inorg. Mater. 55 (1) (2019) 9-13.

[50] D.A. Fischer, I.T. Vargas, G.E. Pizarro, F. Armijo, M. Walczak, The effect of scan rate on the precision of determining corrosion current by Tafel extrapolation: A numerical study on the example of pure Cu in chloride containing medium, Electrochim. ACTA 313 (2019) 457-467.

[51] X.W. Li, T. Shi, B. Li, X.C. Chen, C.W. Zhang, Z.G. Guo, Q.X. Zhang, Subtractive manufacturing of stable hierarchical micro-nano structures on AA5052 sheet with enhanced water repellence and durable corrosion resistance, Mater. Design 183 (2019) 108152.

Table 1 Average granularities and purities of raw materials used in this work.

Powder	Granularity (mesh)	Purity (wt.%)
Ti	400	99.9
TiC	400	99.9
SiC	400	99.0
Al	400	99.0
Ti(C,N)	400	99.0

Figure Captions

Fig. 1. SEM image and XRD pattern of Ti_3SiC_2 powders.

Fig. 2. (a) XRD patterns of Ti_3SiC_2/Ti(C,N) composites sintered at 1400 °C with different Ti(C,N) mass fractions. (b) XRD patterns of Ti_3SiC_2/Ti(C,N) composites sintered with 20 wt% Ti(C,N) at various temperatures. (c) SEM image and (d-e) cross-section SEM images of Ti_3SiC_2/Ti(C,N) composite sintered at 1400 °C with 20 wt% Ti(C,N).

Fig. 3. (a) Measured densities and relative densities of Ti_3SiC_2/Ti(C,N) composites sintered with 20 wt% Ti(C,N) at different temperatures. (b) Measured densities and relative densities of Ti_3SiC_2/Ti(C,N) composites sintered at 1400 °C with various Ti(C,N) mass fractions.

Fig. 4. (a) Relationship between sintering temperature and micro hardness of Ti_3SiC_2/Ti(C,N) composites with 20 wt% Ti(C,N). (b) Micro hardness of Ti_3SiC_2/Ti(C,N) composites sintered at 1400 °C with different Ti(C,N) mass fractions.

Fig. 5. (a) Instantaneous friction coefficients versus friction time for Ti_3SiC_2/Ti(C,N) composites with different Ti(C,N) contents at a low speed of 0.1 m/s and a light load of 5 N. (b) Instantaneous friction coefficients versus time for Ti_3SiC_2/Ti(C,N)

28

composites with different Ti(C,N) contents at a high speed of 0.4 m/s and a heavy load of 20 N.

Fig. 6. (a) Friction coefficients and (b) wear rates versus Ti(C,N) contents for composites at different speeds and loads.

Fig. 7. SEM images of frictional composites with Ti(C,N) contents of (a) 5 wt% and (b) 20 wt% under a low speed (0.1 m/s) and light load (5 N) condition.

Fig. 8. SEM images and EDS spectra of frictional composites with Ti(C,N) contents of (a, c) 5 wt% and (b, d) 20 wt% under a high speed (0.4 m/s) and heavy load (20 N) condition.

Fig. 9. (a) Friction coefficients and (b) wear rates versus applied loads for composites with 20 wt% Ti(C,N) at different rotation speeds.

Fig. 10. SEM images and EDS spectra of frictional composites with 20 wt% Ti(C,N) and 20 N load at speeds of (a, c) 0.1 m/s and (b, d) 0.2 m/s.

Fig. 11. SEM images, enlarged images and EDS spectra of frictional composites with 20 wt% Ti(C,N) and 0.3 m/s rotation speed at loads of (a, c, e) 5 N and (b, d, f) 15 N.

29

Fig. 12. Relationship between mass increments (ΔW) and oxidation cycle times of Ti$_3$SiC$_2$/Ti(C,N) composites with 20 wt% Ti(C,N) at different oxidation temperatures.

Fig. 13. (a) XRD patterns of oxide layers on Ti$_3$SiC$_2$/Ti(C,N) composites after 40 oxidation cycles at different temperatures. (b) XRD patterns of oxide layers on Ti$_3$SiC$_2$/Ti(C,N) composites after various oxidation cycles at 1000 °C.

Fig. 14. SEM images of oxide layers on Ti$_3$SiC$_2$/Ti(C,N) composites after 40 oxidation cycles at (a) 800 °C, (b) 1000 °C and (c) 1200 °C. EDS spectra of oxide layers on Ti$_3$SiC$_2$/Ti(C,N) composites after 40 oxidation cycles at (d) 800 °C and (e) 1200 °C.

Fig. 15. Cross-section SEM images of oxide layers on Ti$_3$SiC$_2$/Ti(C,N) composites after 40 oxidation cycles at (a) 800 °C, (b) 1000 °C and (c) 1200 °C.

Fig. 16. (a) Polarization curves and (b) electrochemical impedance spectra of Ti$_3$SiC$_2$/Ti(C,N) composites sintered at 1400 °C with various Ti(C,N) mass fractions in 3.5 wt% NaCl solution.
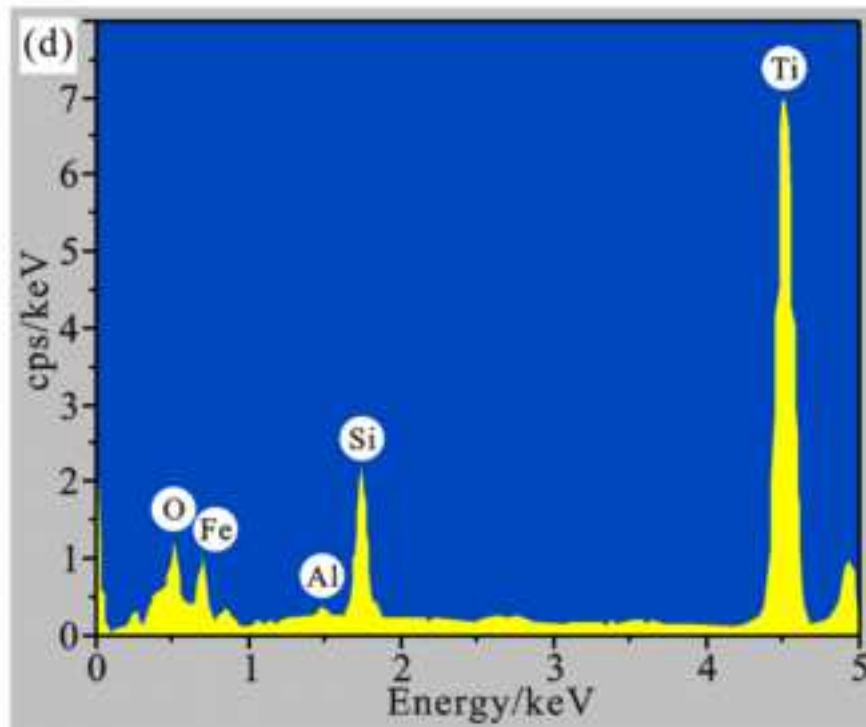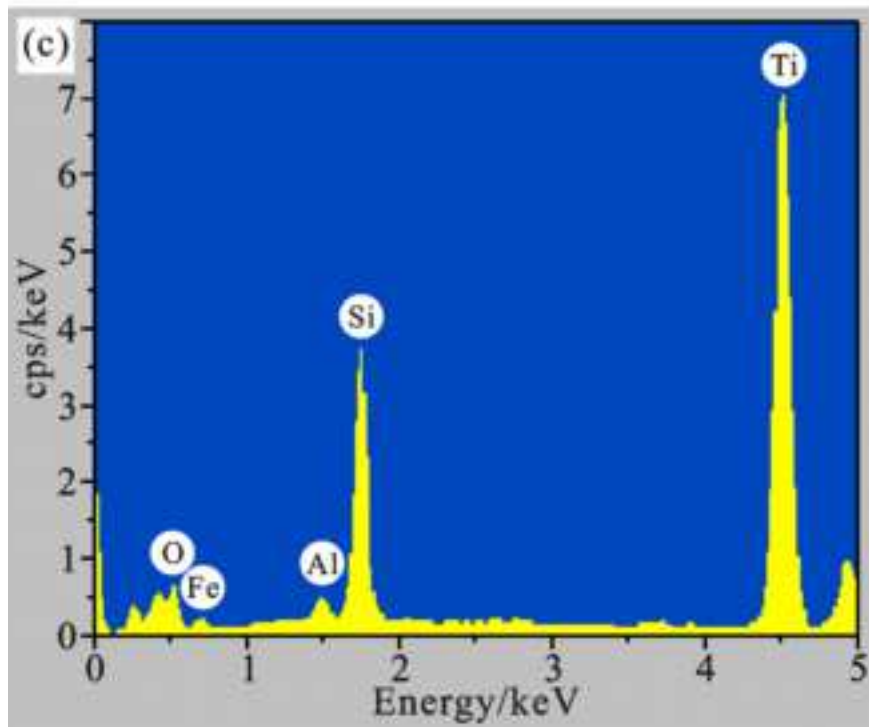
Figure 1
[Click here to download high resolution image](#)
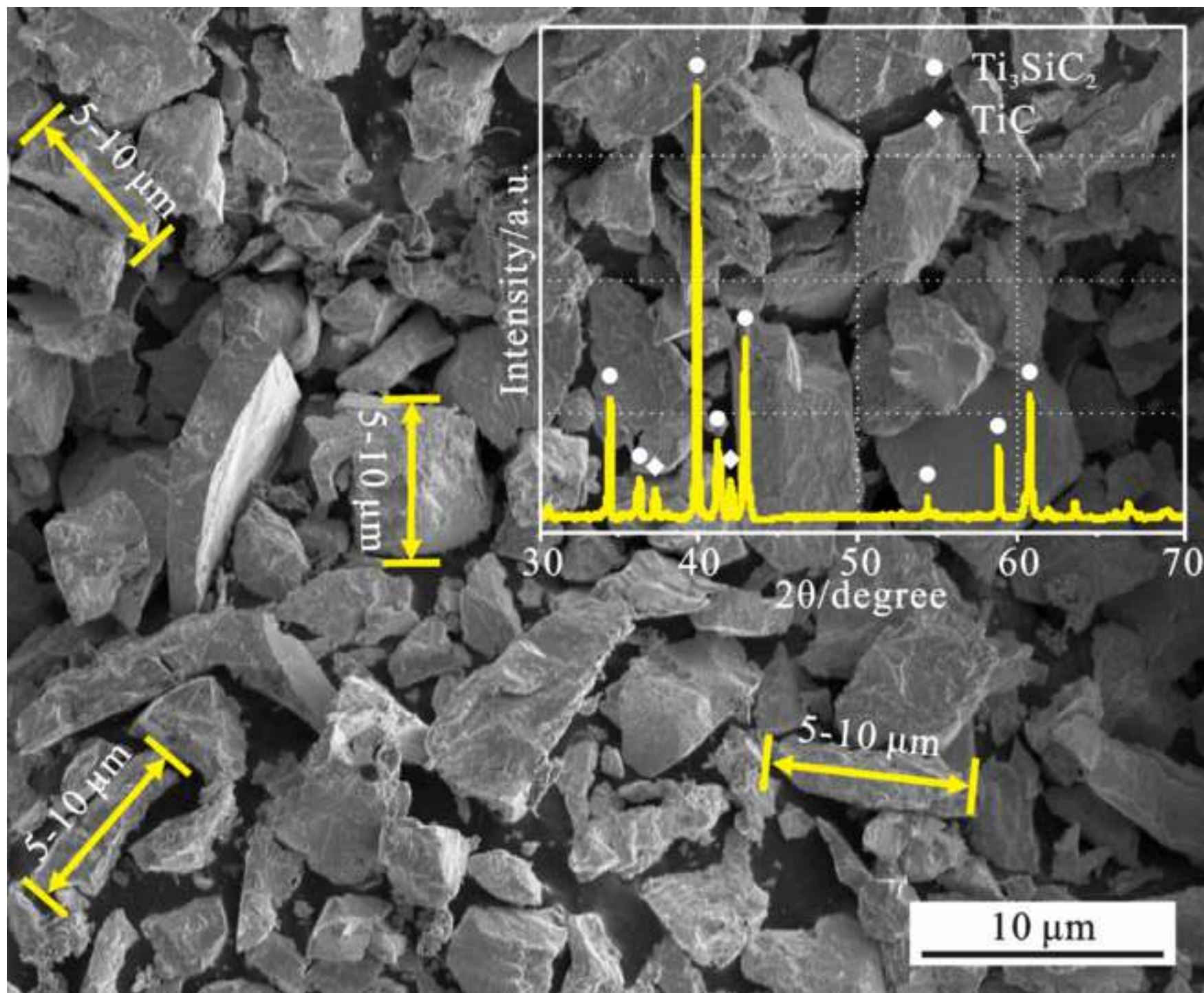
Figure 1

Figure 2
Click here to download high resolution image
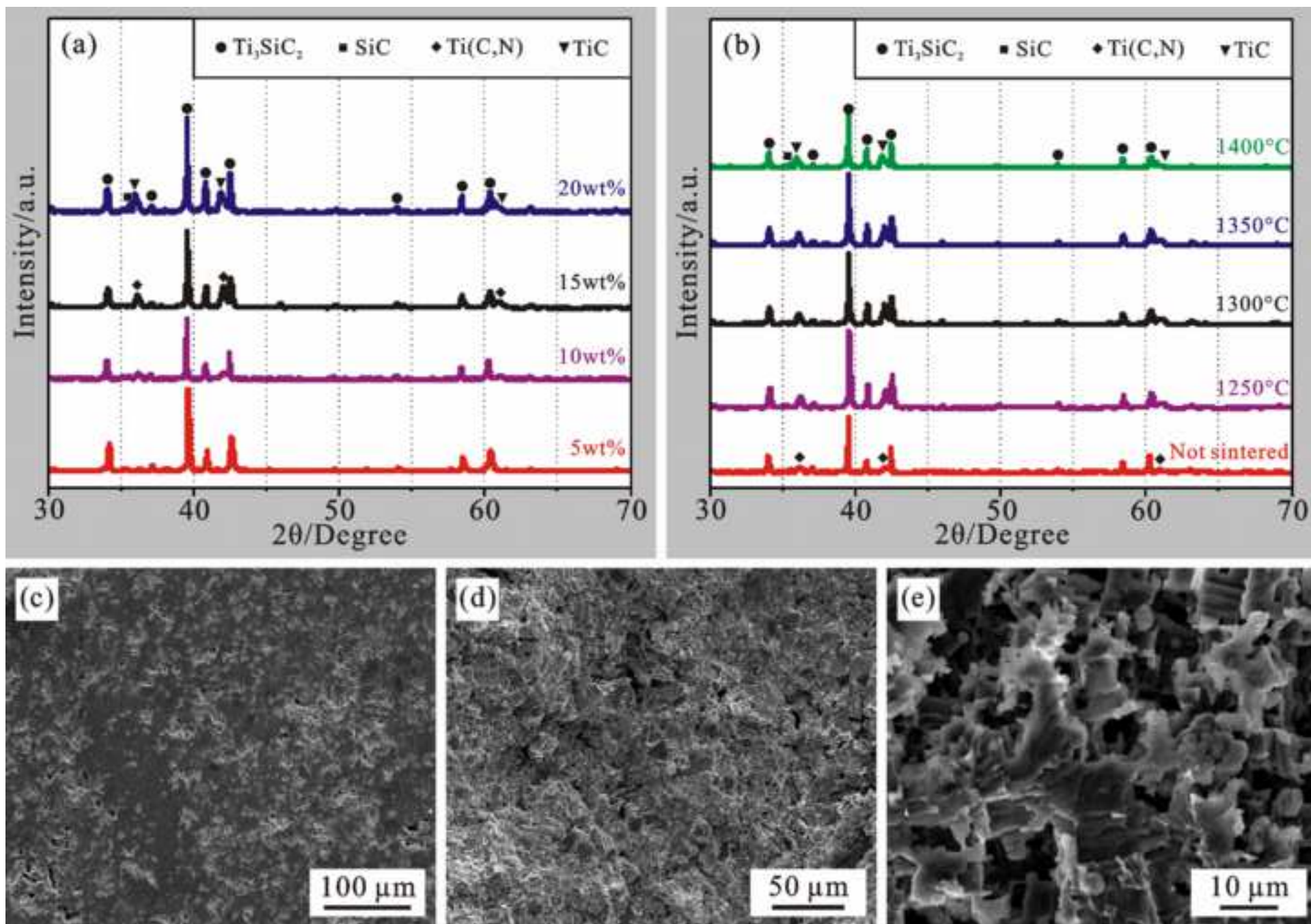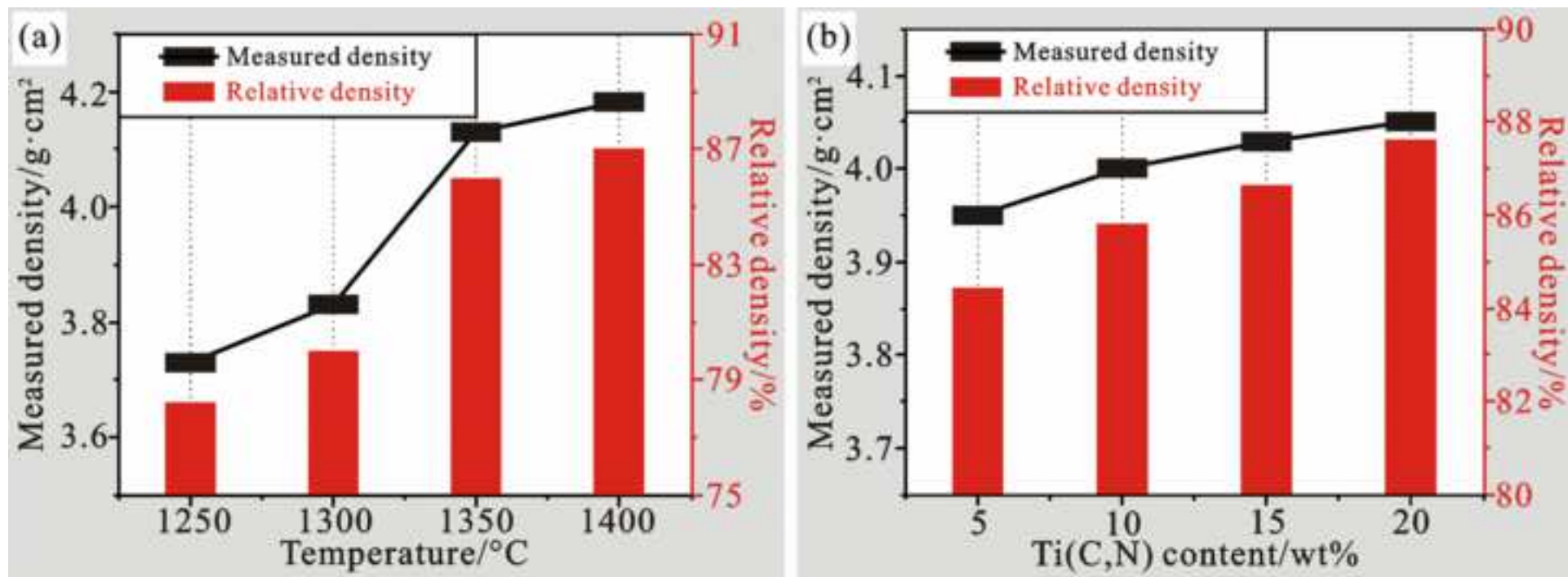
Figure 4
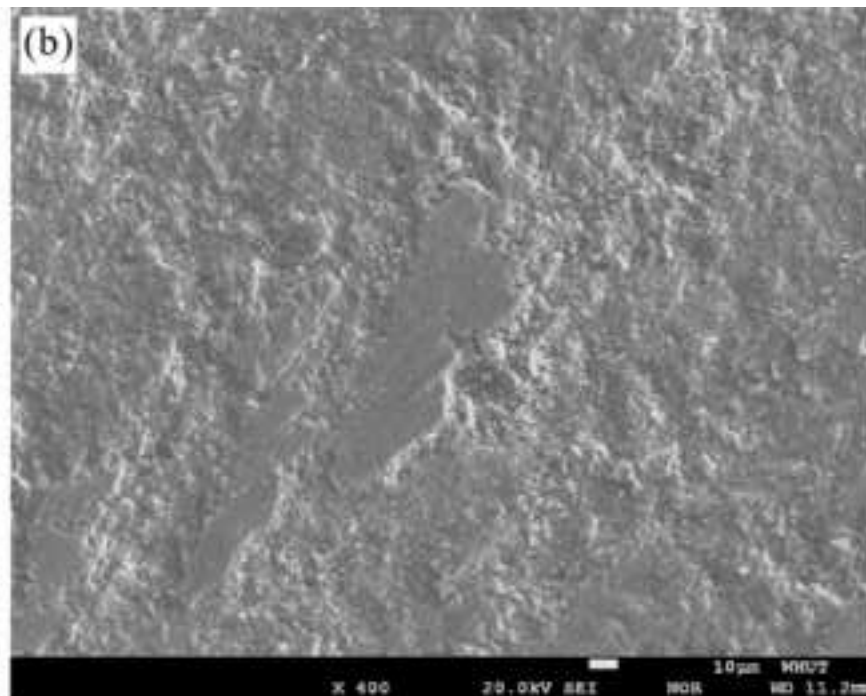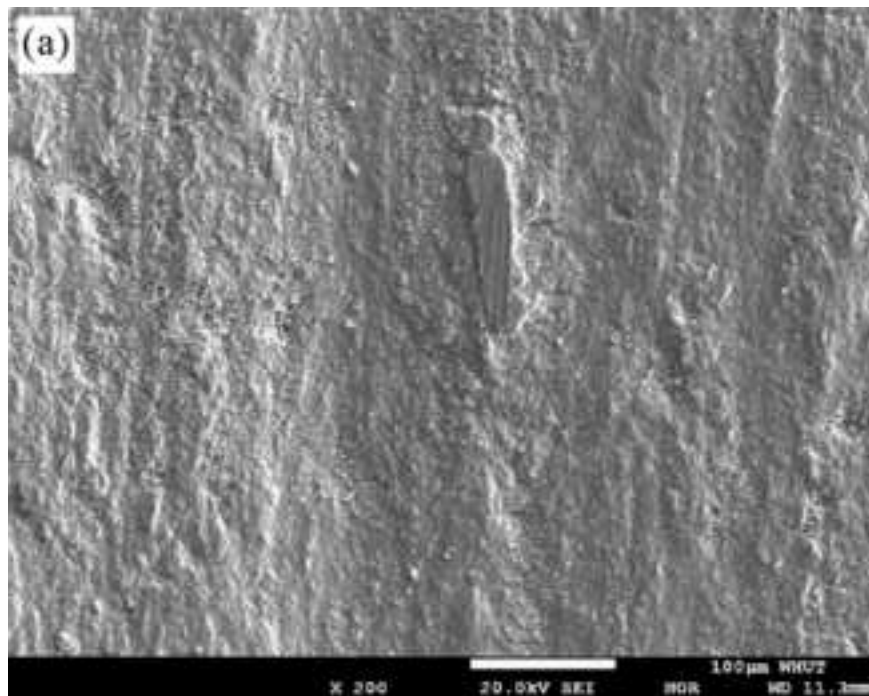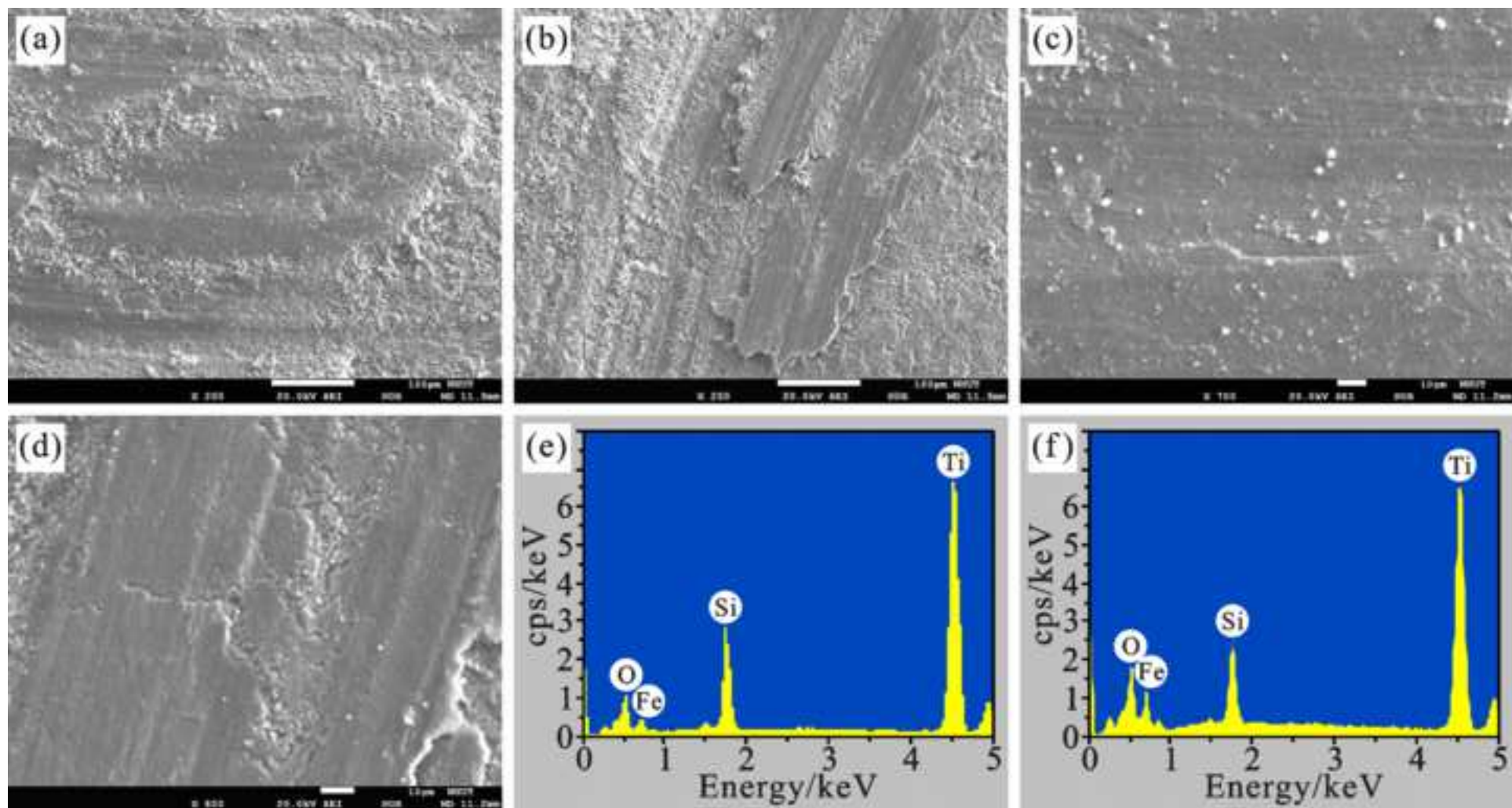**Click here to download high resolution image**
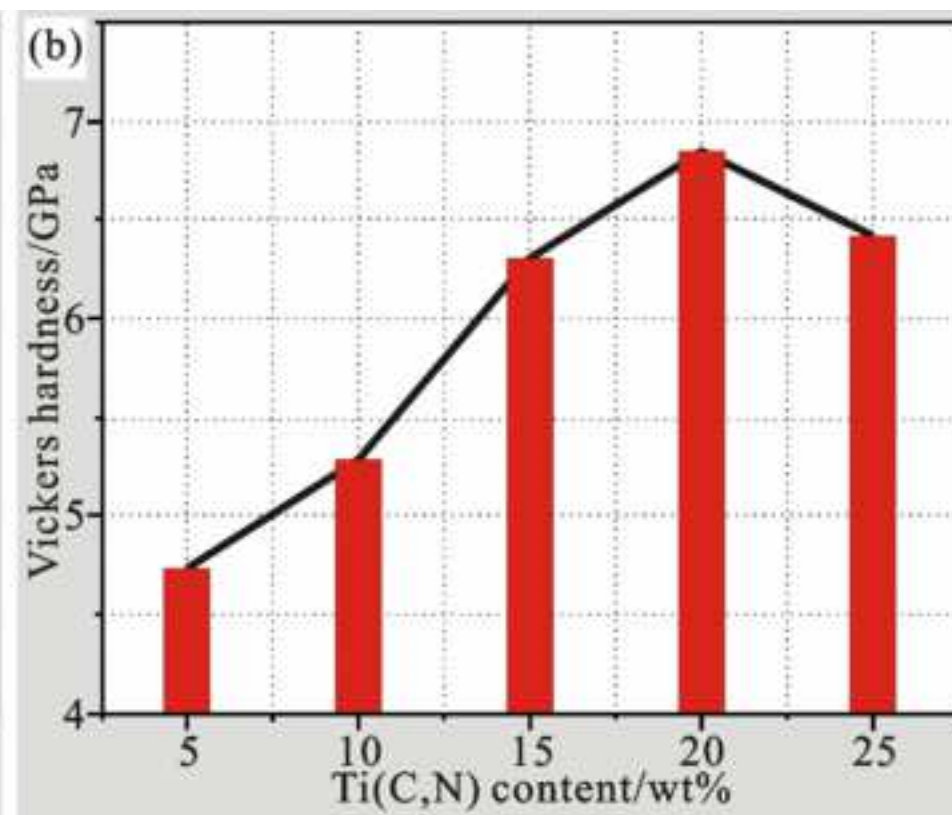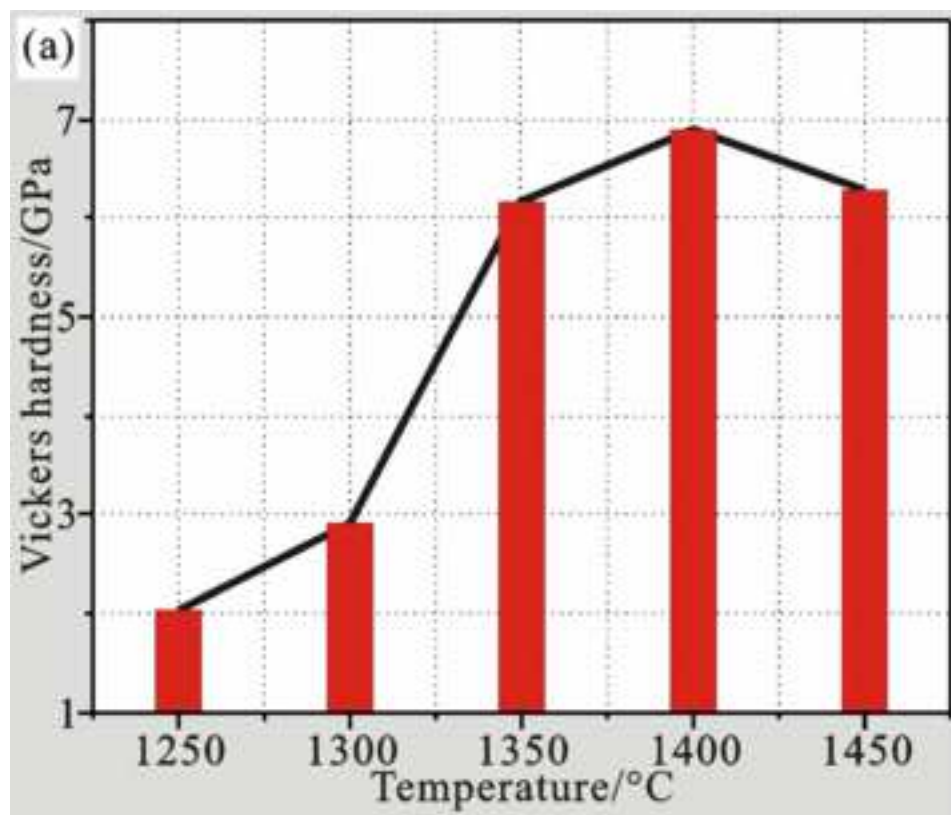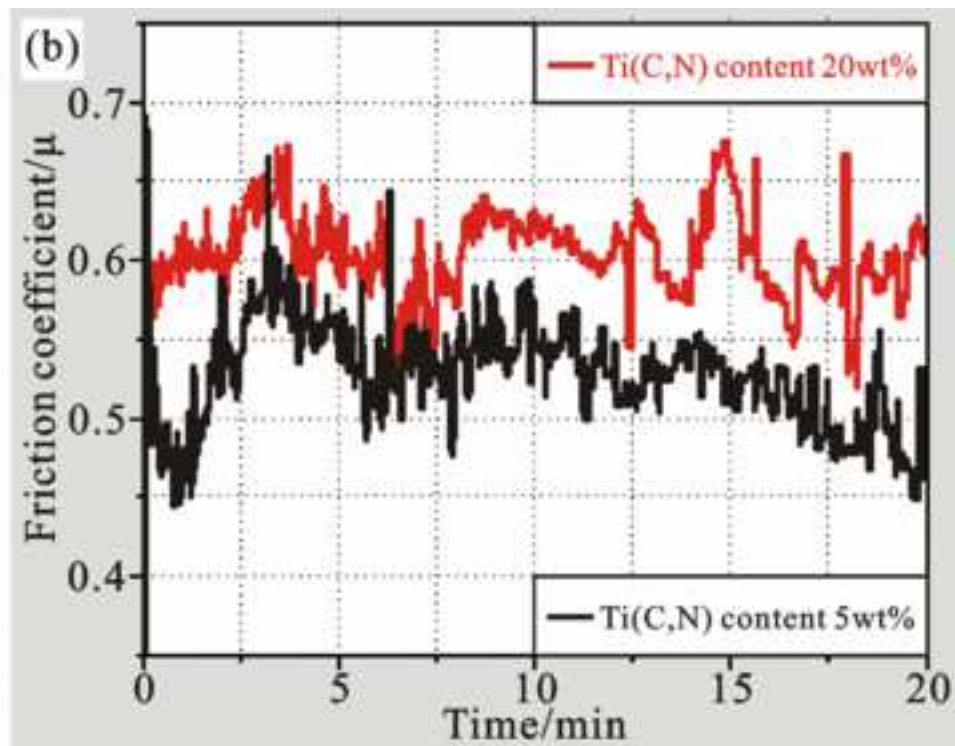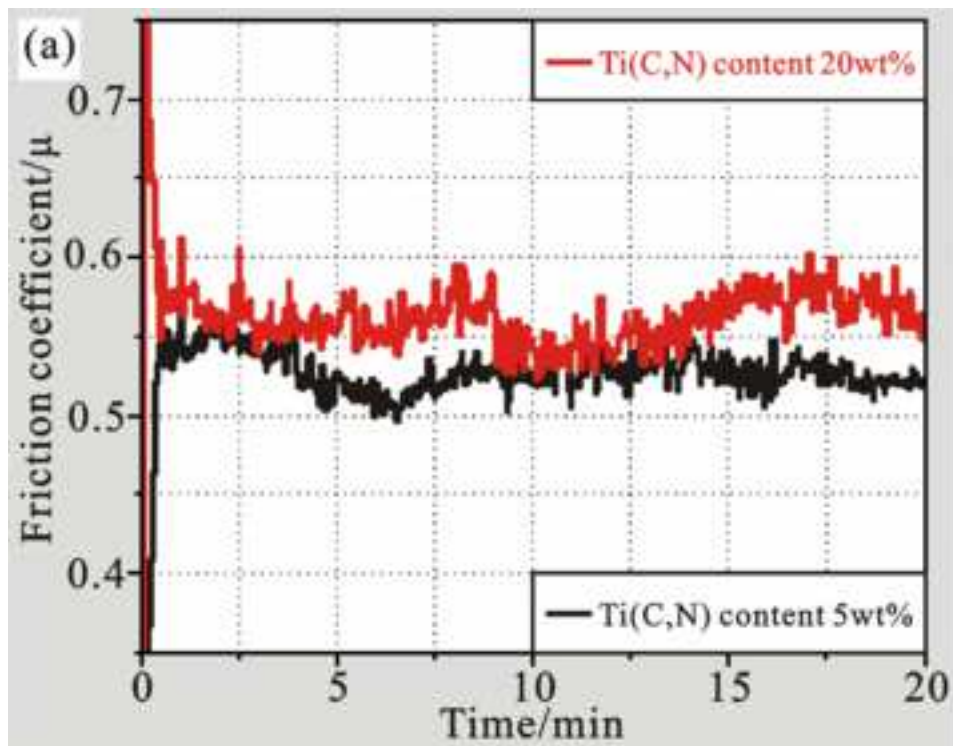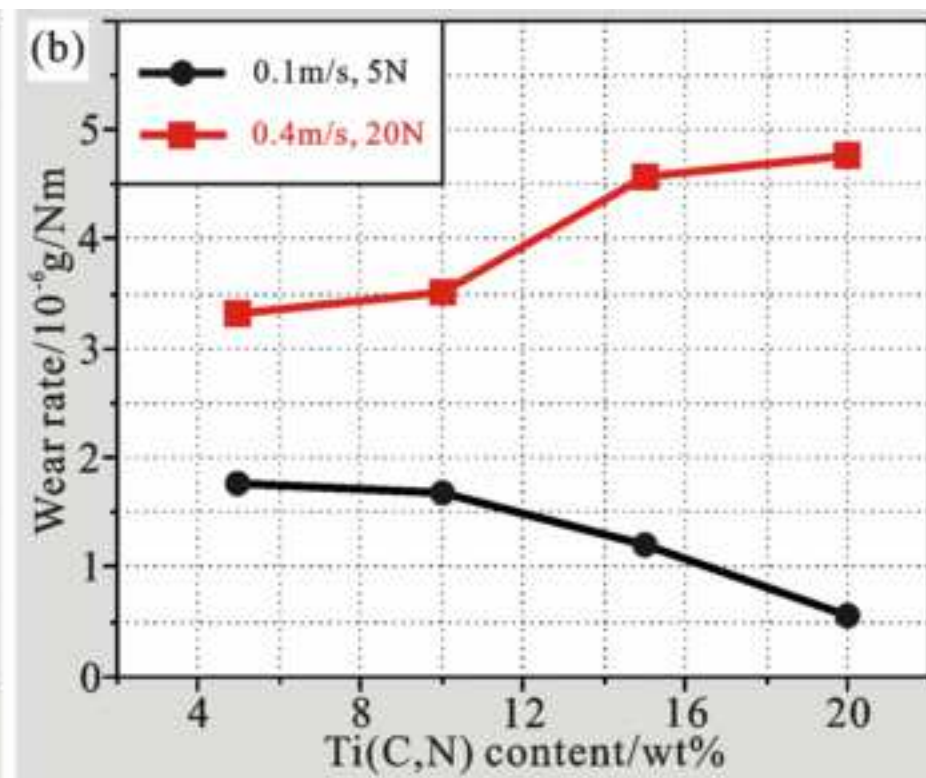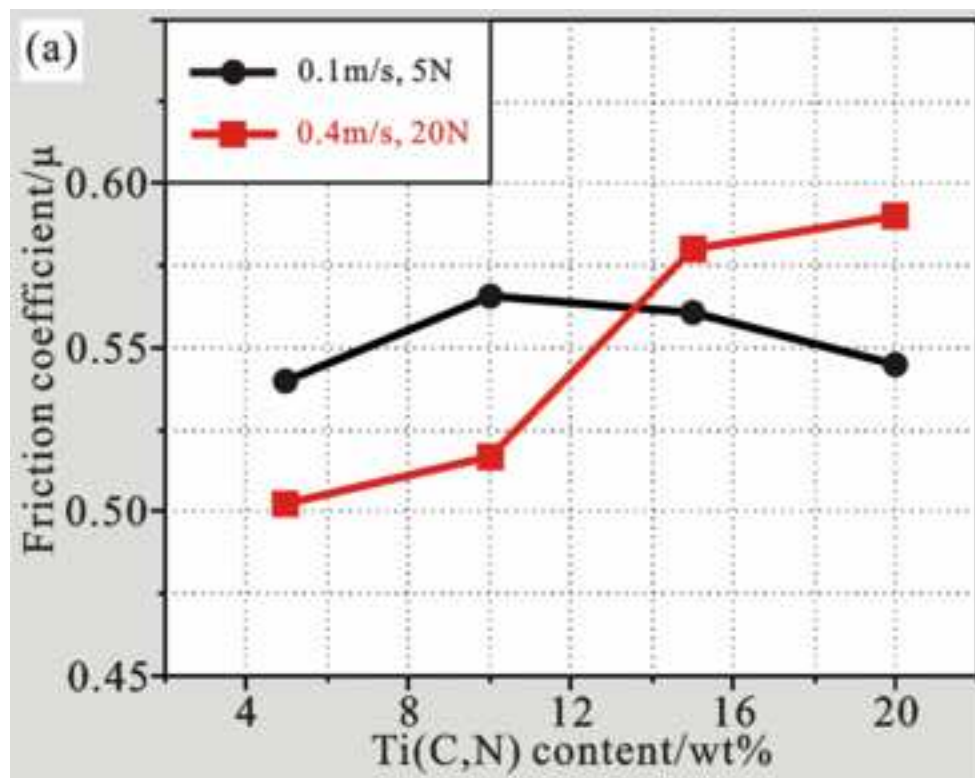
Figure 7
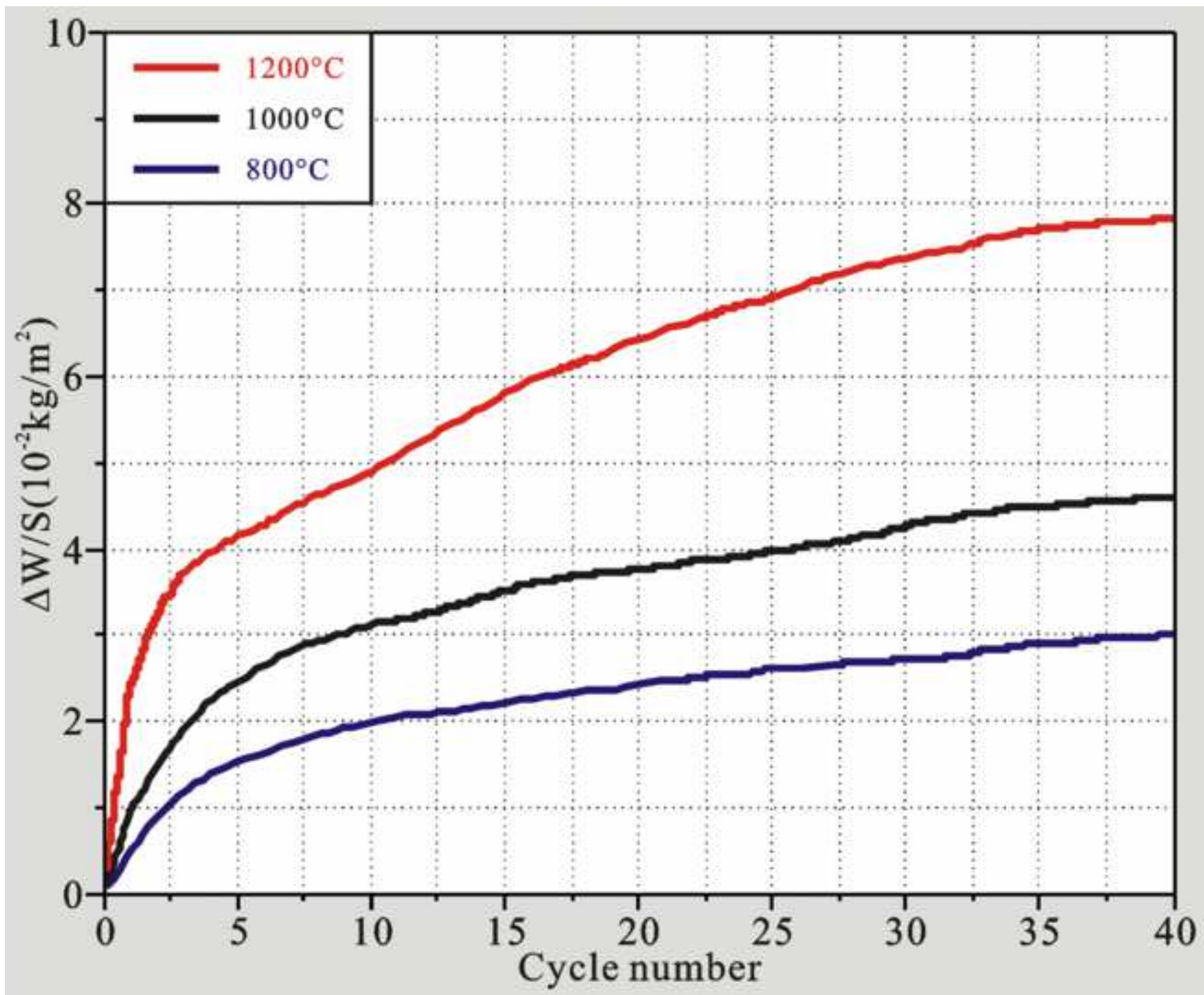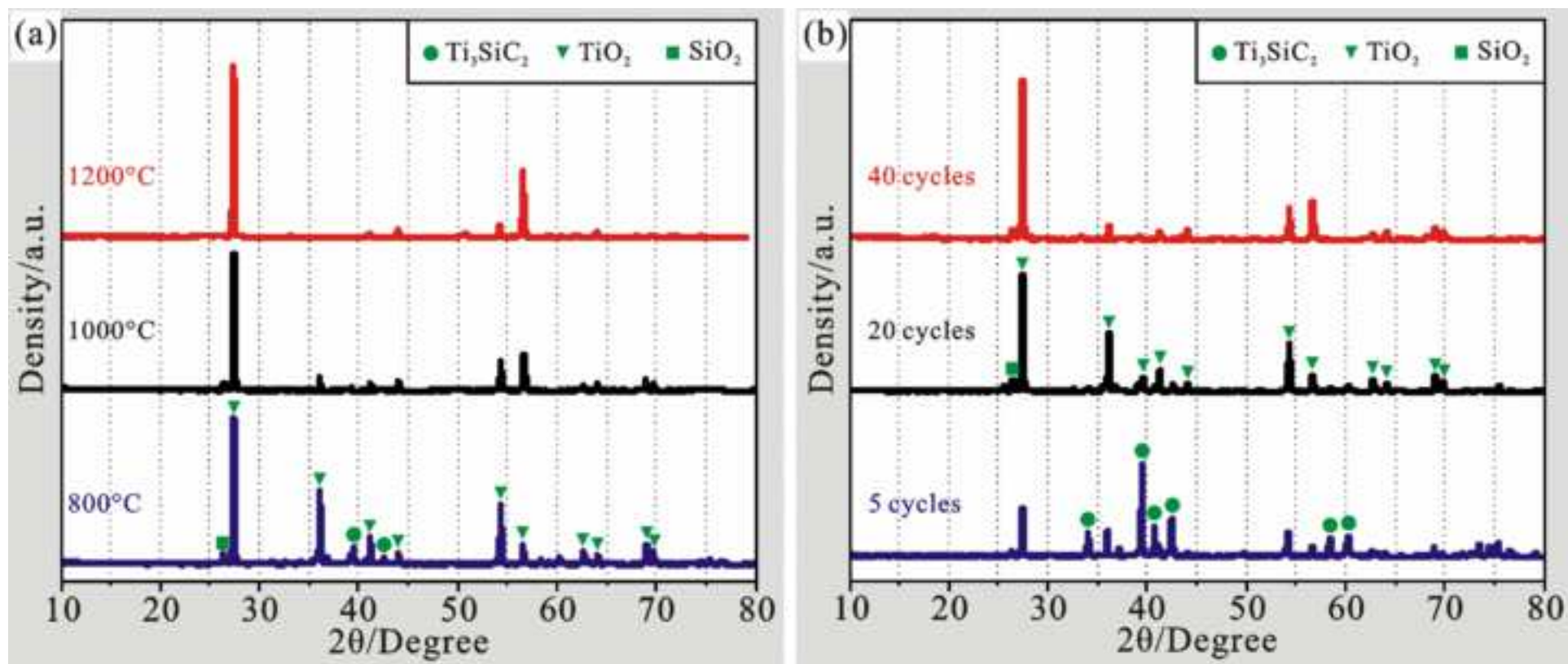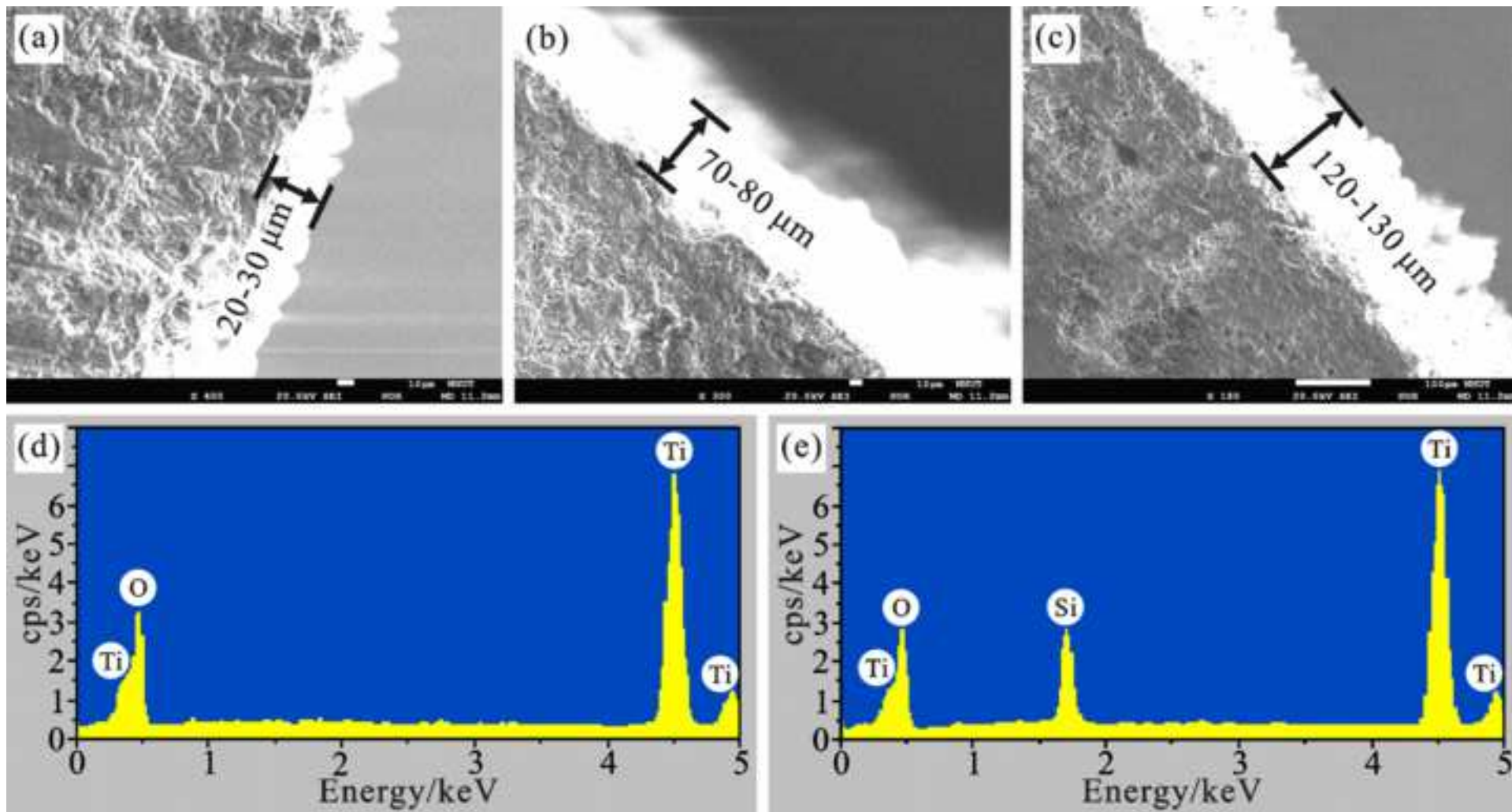[Click here to download high resolution image](#)
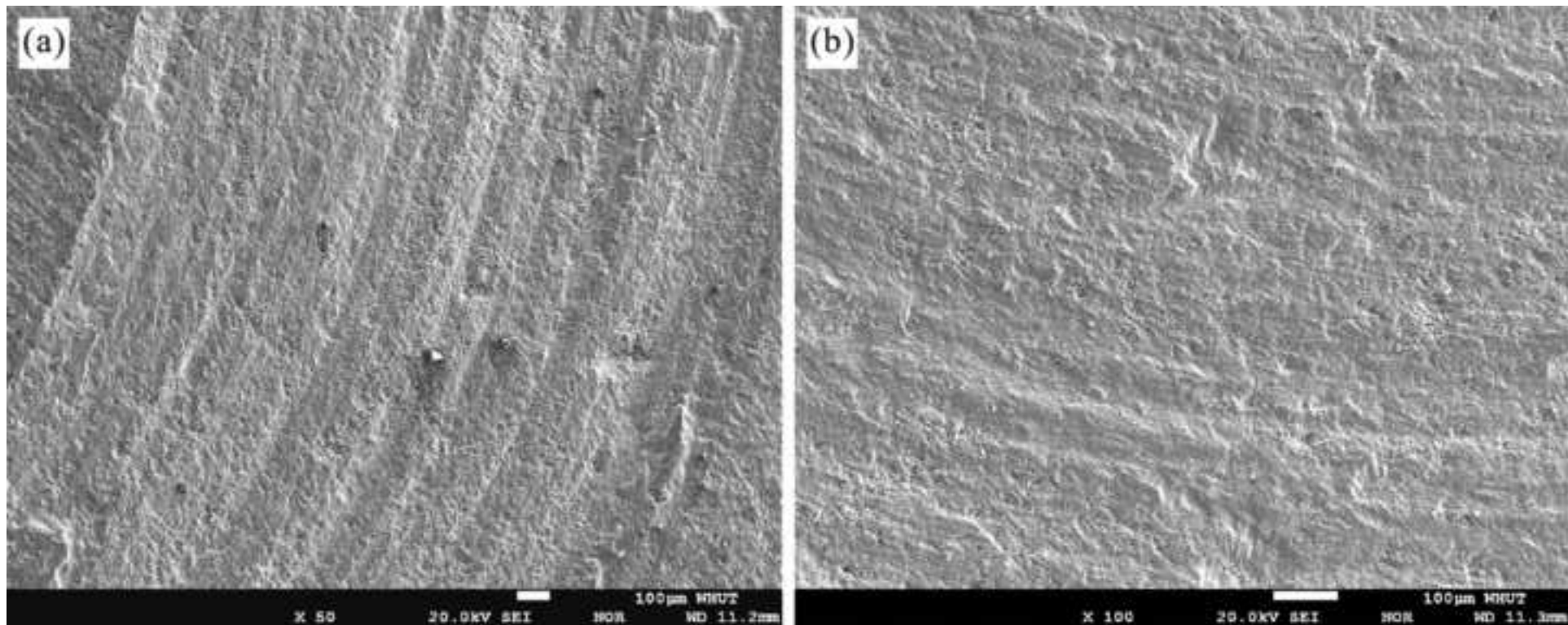
Figure 8
Click here to download high resolution image
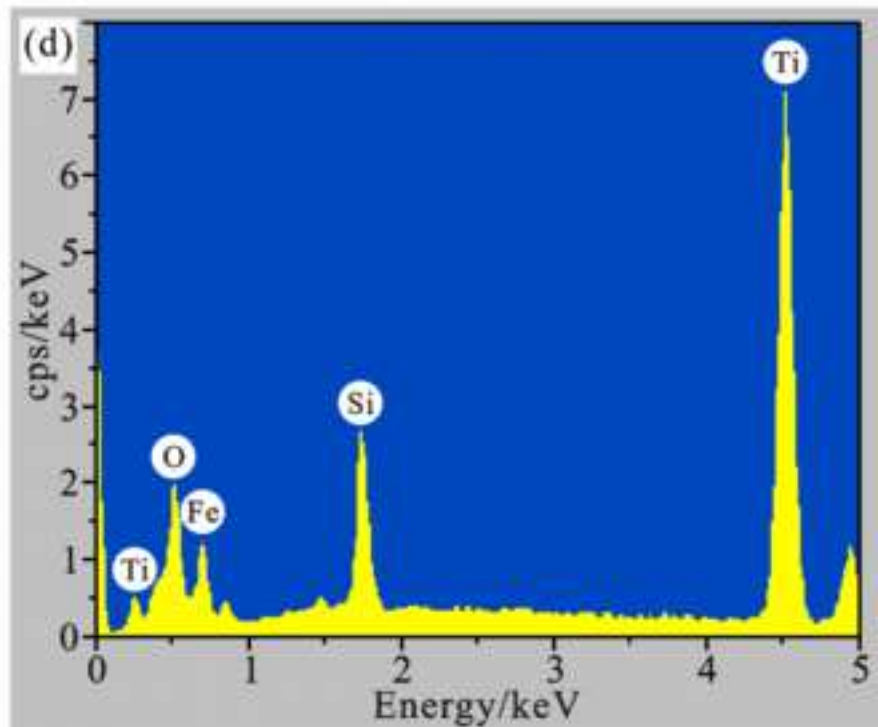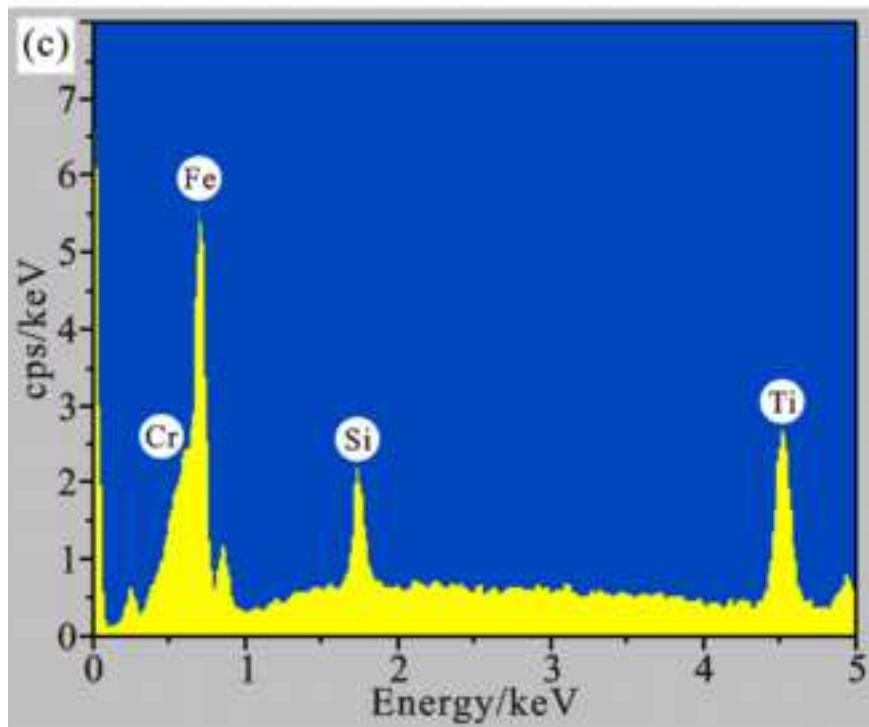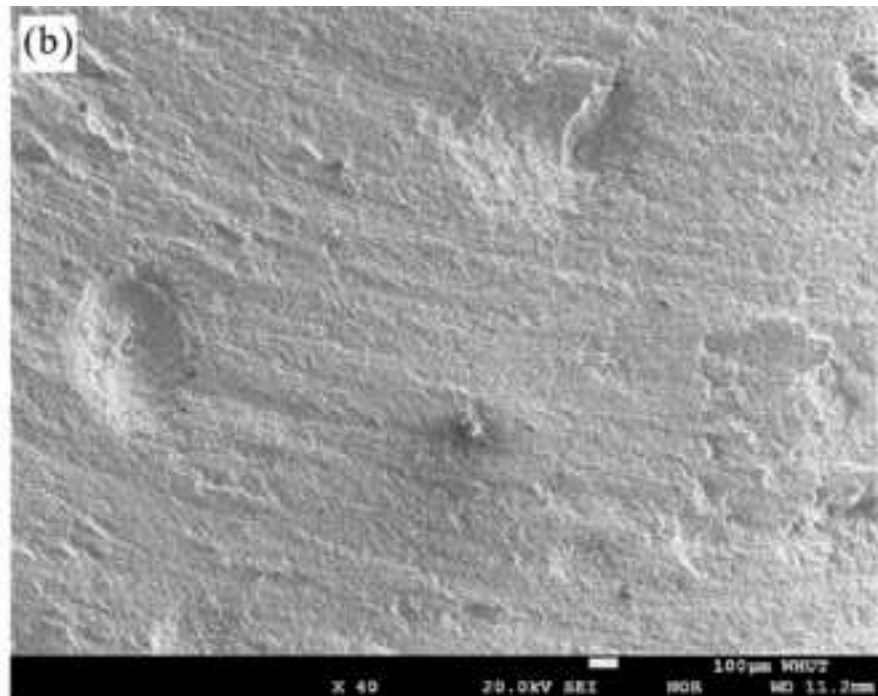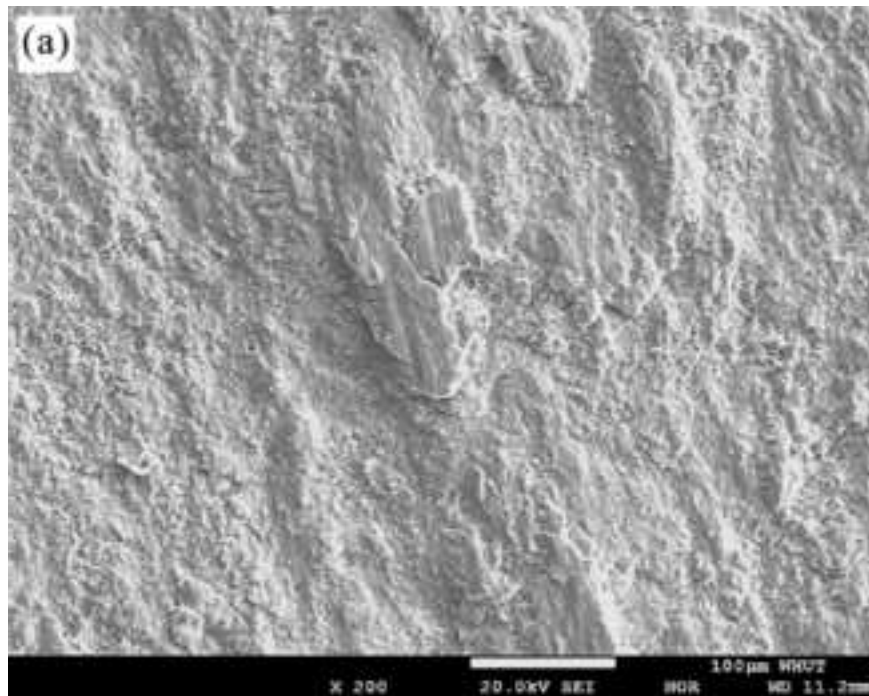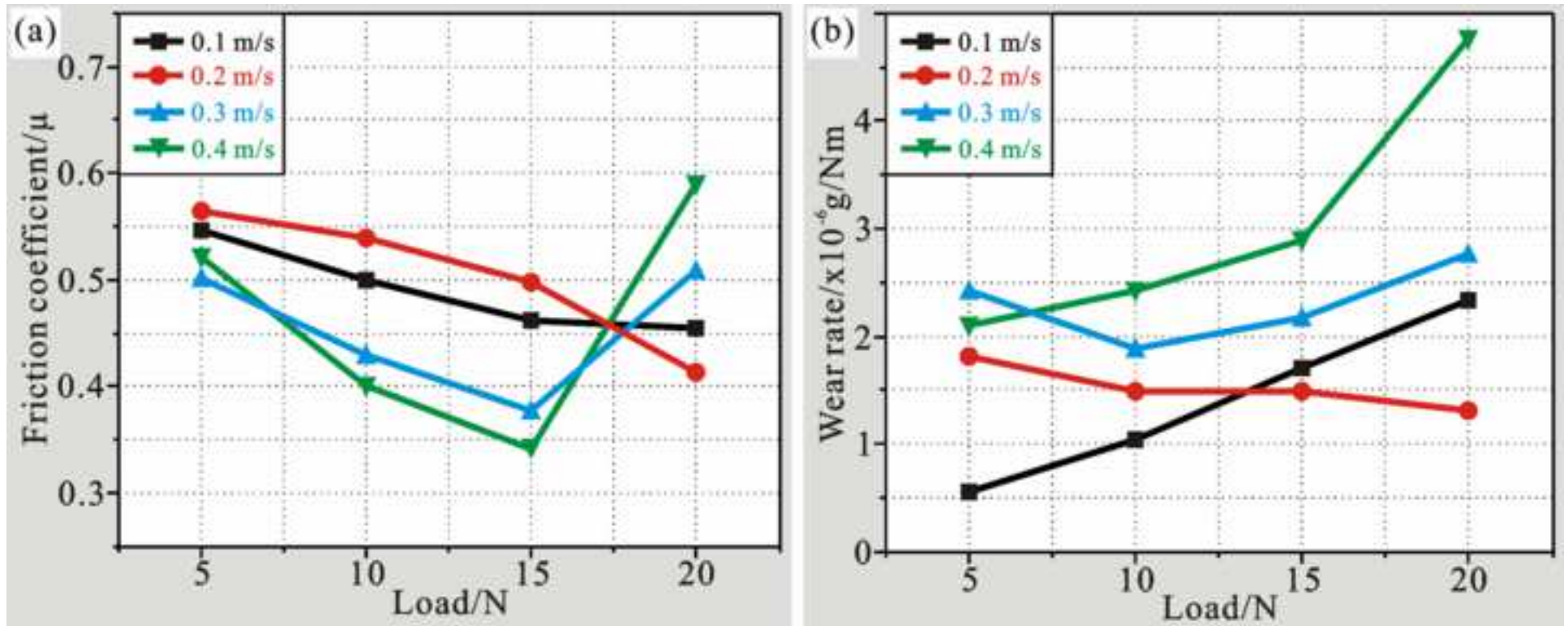
Figure 10
[Click here to download high resolution image](#)

Figure 11
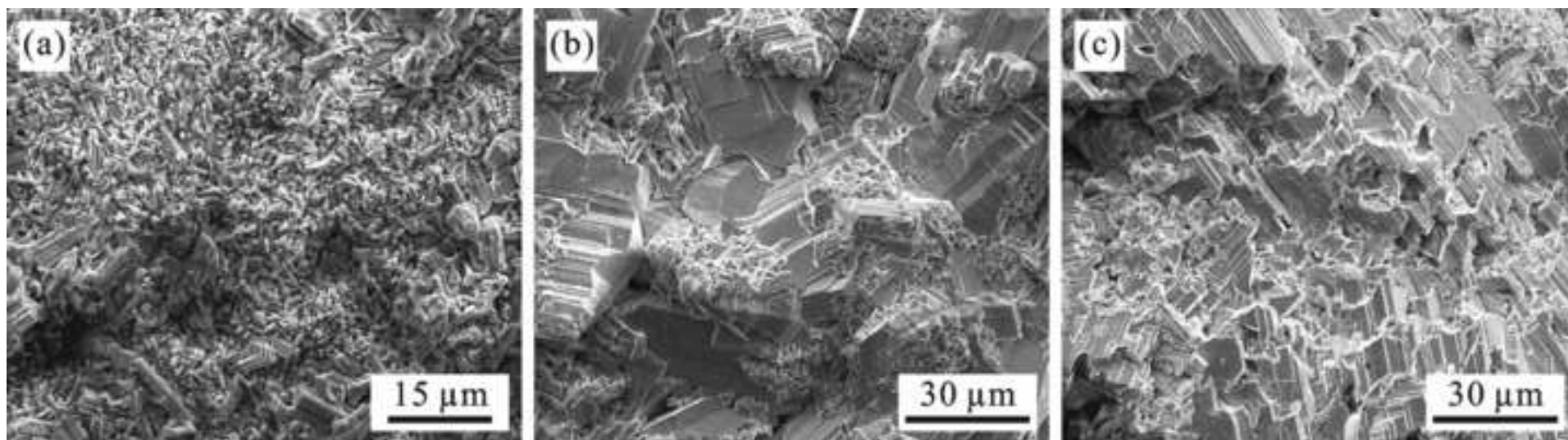[Click here to download high resolution image](#)

Figure 12
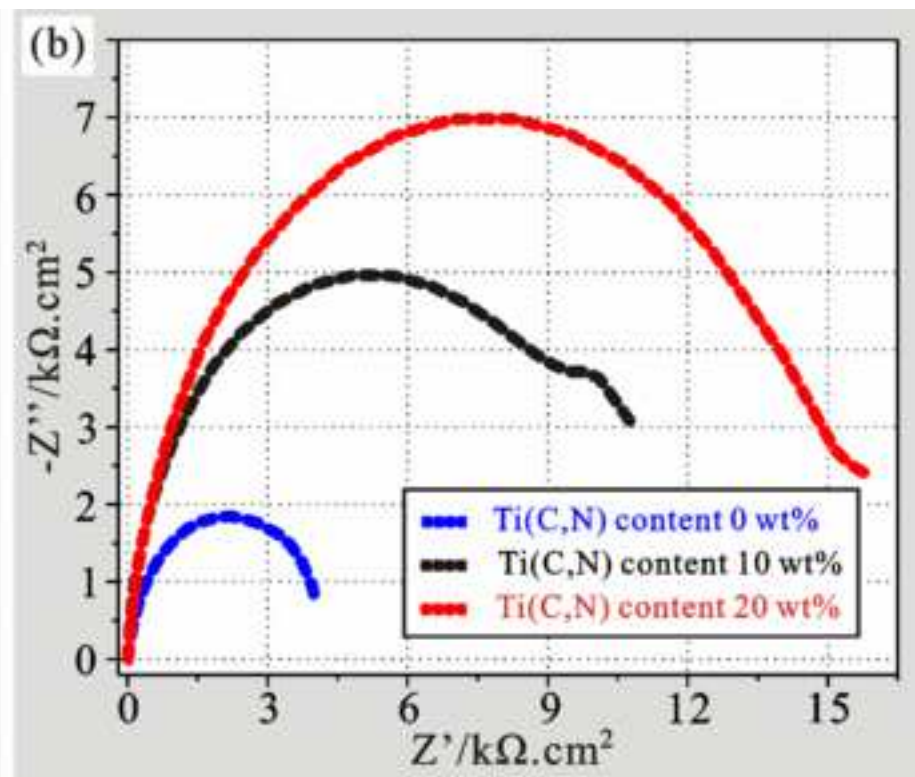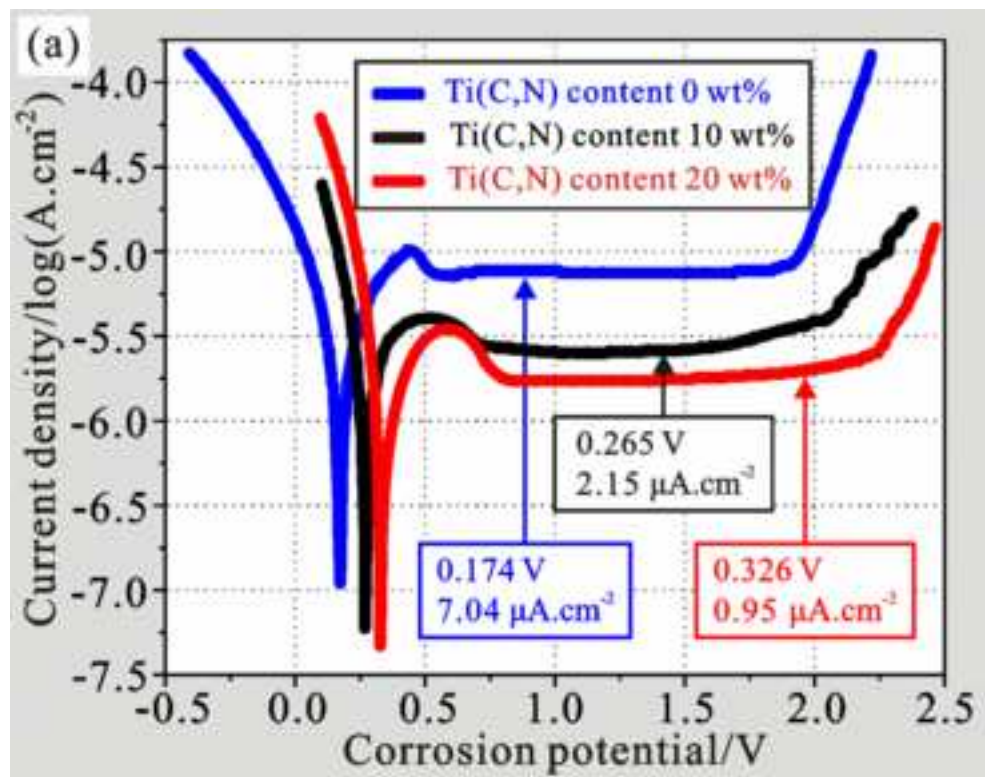**Click here to download high resolution image**

Figure 14
Click here to download high resolution image

Figure 15

Figure 16

Declaration of interests

■The authors declare that they have no known competing financialinterestsor personal relationships that could have appeared to influence the work reported in this paper.

☐The authors declare the following financial interests/personal relationships which may be considered as potential competing interests: